Title

Molecular mechanisms of thickness-dependent water desalination in polyamide reverse-osmosis membranes

Authors

He, Jinlong
Arbaugh, Tom
Nguyen, Danh
et al.

Publication Date

2023-05-01

DOI

10.1016/j.memsci.2023.121498

Molecular mechanisms of thickness-dependent water desalination in polyamide reverse-osmosis membranes

Journal of Membrane Science

Jinlong He [a,b], Tom Arbaugh[c], Danh Nguyen[b], Weikang Xian[b], Eric M. V. Hoek[d,e], Jeffrey R McCutcheon[f], and Ying Li[a,b*]

[a] Department of Mechanical Engineering, University of Connecticut, Storrs, Connecticut 06269, United States

[b] Department of Mechanical Engineering, University of Wisconsin-Madison, Madison, Wisconsin 53706 - 1572, United States

[c] Department of Physics, Wesleyan University, Middletown, Connecticut 06459, United States

[d] Department of Civil & Environmental Engineering, California NanoSystems Institute, and Institute of the Environment & Sustainability, University of California, Los Angeles, Los Angeles, California, United States

[e] Energy Storage & Distributed Resources Division, Lawrence Berkeley National Lab, Berkeley, California, USA

[f] Department of Chemical & Biomolecular Engineering, Center for Environmental Sciences and Engineering, University of Connecticut, Storrs, Connecticut 06269, United States

[*]**Corresponding Author: Email: yli2562@wisc.edu; Phone: +1-608 265 0577; Fax: +1-608 890 3966**

ABSTRACT

Using non-equilibrium molecular simulations, we systematically elaborate the relationships among synthesis (membrane's thickness and morphology), atomic-scale transport mechanism, and separation performance (permeability and selectivity) for 3D-printed polyamide (PA) membranes. Results indicated that water diffusion, swelling ratio, water flux, and water permeance proportionally decrease with increasing membrane thickness (4.0 to 32.5 nm). PA membranes with different thicknesses can achieve almost 100% salt rejection over the simulation time. Importantly, water permeability exponentially decreases with increasing thickness, and 15 nm is identified as the critical membrane thickness for efficient water transport. The discontinuous water-available space spreads all over PA membranes with thicknesses greater than 5 nm, allowing water molecules to jump by way of the temporary open-and-close pores. However, the connected water-usable space exists in PA membranes with thicknesses below 5 nm, offering the continuous channels to dominate water transport. More significantly, pore distribution is more homogeneous as the thickness increases. The applied high pressures can lead to membrane compaction during reverse osmosis and the thicker membranes show a lower compression ratio. In short, these investigations provide molecular insights for effectively designing and manufacturing PA membranes for water desalination and treatment at the molecular level.

Keywords: polyamide membrane, thickness-dependence, pore size distribution, non-equilibrium molecular dynamics, water desalination

Graphical Abstract:

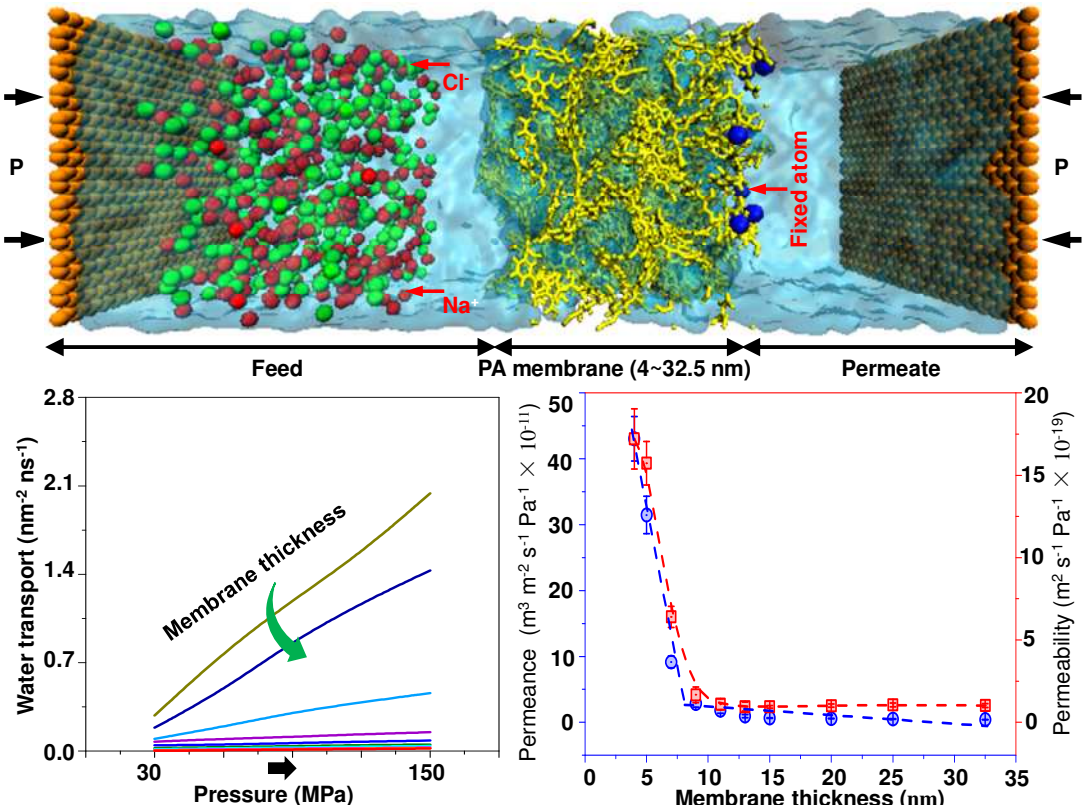

ABBREVIATIONS:

HPRO: High-pressure reverse osmosis
PA: Polyamide
EMD/NEMD: Equilibrium/Non-Equilibrium molecular dynamics
PBC: Periodic boundary conditions
MPD: m-phenylenediamine
CD: Cross-linking degree
TMC: Trimesoyl chloride
SD: Solution-diffusion
MSD: Mean square displacement
CL: Confined layer
BL: Bulk layer
TL: Transition layer
PSD: Pore size distribution

1. Introduction

Providing access to clean water is an essential public necessity fundamental to agriculture, industrialization, human consumption, and urbanization [1]. Through decades of efforts, polymeric membranes-based reverse osmosis (RO) processes reveal relatively excellent membrane properties (*e.g.*, permeability and selectivity) as well as high-energy efficiency for supplying clean water [2-4]. Generally, a kind of polyamide (PA)-based composite membranes are used for water desalination, purification and treatment. Using different manufacturing technologies, such as 3D-printing, molecular layer-by-layer, and interfacial polymerization, PA membranes are easily fabricated according to two reactants (m-phenylenediamine, or named MPD; and trimesoyl chloride, or named TMC). Despite PA RO membranes being extensively used for water treatment, the discovery of technique-renovation materials, the accelerated manufacturing process, optimized energy efficiency, and enhanced separation performance remain a great challenge. To address these challenges, it is important to provide a comprehensive investigation for the molecular level structure-properties relationship (*e.g.*, thickness and MPD/TMC ratio), and water transport mechanisms within the PA membranes.

Water and solute pass through PA RO membranes is usually characterized using solution-diffusion (SD) mechanism [5]. This mechanism assumes that water and ions first partition into membranes, then diffuse within membranes, and finally permeate through the membranes. The effects of membrane properties, such as fractional free volume, degree of cross-linking (DC), chemical structure and thickness, are not well studied. One previous study uncovered how MPD/TMC ratio and DC affect 3D-printed PA membranes' performance [6]. In addition, controlling membrane thickness is another strategy to regulate RO membrane permeance and selectivity. This method has been widely used in ultrathin carbon nanosheets [7] and ultrathin protein-based membranes [8] to enable ultrafast water permeation by reducing the membrane thickness.

In previous studies on PA membranes for RO (**Table 1**), it can be found that most reports from experiments and simulations explore water permeability and ion selectivity at a specific membrane thickness. For example, Zhang et al. [9] reported PA nanofilms with controllable thickness (6.0 to 15.5 nm) formed by IP across the free organic/aqueous interface. Results indicated that these membranes present a nonlinear decrease in water permeance with increasing thickness up to 8 nm. For PA nanofilms with thicknesses from 8 to 15.5 nm, the water

permeance linearly decreases with increasing thickness, leading to nearly constant water permeability. Thus, 8 nm is considered to be the critical thickness for these PA nanofilms formed by the IP. This investigation indicates that water transport diffuses more slowly in thicker membranes, then tended to be stable after the thickness increases to a threshold. Using the IP method, the RO membrane morphology is capable of changing from smooth to crumpled configuration, where the crumpled morphologies are caused by nanofilms' stacking and folding. Therefore, the crumpled membranes may have the same intrinsic thickness as the 8 nm-thick smooth nanofilms (or 20 nm measured by Yan et al. [10]), even when the apparent thickness is larger than 100 nm. They state that the point of enhancing the RO membrane's permeance is to reduce its inherent nanofilm thickness. Starting from this direction, a more easily controllable mLBL assembly approach has been advanced to fabricate smooth PA nanofilms [11]. With this technique, Mulhearn et al. [12] manufactured a series of highly cross-linked PA membranes with various thicknesses (5.0~100.0 nm). It shows that the rejection is poor for PA films that are thinner than 8.0 nm, increase from 88.0% at 8.0 nm to 97.0% at 15.0 nm, and are not dependent upon thickness above 15 nm. Therefore, 15.0 nm is discerned as a critical thickness for efficient water desalination.

Although a wide range of thicknesses for PA membranes has been explored by experiments, these studies mainly focus on permeability and rejection for RO membranes formed with IP or mLBL. It is not clear how the water transport and ion rejection mechanisms are influenced by the PA membrane's thickness or morphology. Recently, molecular dynamics (MD) simulations have demonstrated that manufacturing methods could dramatically affect the membrane's properties [13]. Thus, these existing investigations still cannot simultaneously answer how thicknesses affect membrane performance, microstructure, transport mechanism, and structural features for PA membranes manufactured by IP and mLBL, not to mention that by 3D-printing. In comparision with the three manufacturing methods, 3D-printing has the capability to fabricate TFC membranes from any solution-processable polymer as well as enhance permeability without sacrificing selectivity [14, 15]. Consequently, it is critical to systematically expound the structure-properties relationship of 3D-printed PA membranes, particularly, the influence of the membrane's thickness and morphology.

Table 1 Summary of prior computational and experimental studies on PA membranes

Polymer system	Method (computation/experiment)	Density (g cm^{-3})	wt% H_2O	Mechanism	Thickness (nm)	Ref.
PA	CVFF (BioSym)	~1.3	~23	Jump [a]	~3	[16, 17]
PA	CHARMM	~1.4	~23	NR [c]	~5-9	[18, 19]
PA	CCA CG	NA	NA	NA [d]	~2-10	[20]
PA	DLPOLY/OPLS-AA	~1.34	~23	NR	~20	[21, 22]
PA	GROMACS	~1.3	~26-29	NR	~20-30	[23, 24]
PA	DLPOLY/AMBER99	~1.32	~23	Smooth [b]	~8	[25]
PA	NAMD/GAFF/NEMD	~1.38	~23	Jump	~5	[26, 27]
PA/nxL	LAMMPS/CVFF	~1.38	~23	NR	~7	[28]
PA	LAMMPS/CVFF	~1.35	NR	NR	~7	[29]
PES	Cerius2/CVFF/CLAYFF	~1.30	NR	NR	~3	[30]
PA/Si Wafer	NA	NR	NR	NA	~30	[31]
PA/CNT	DLPOLY	NR	NR	NA	~3	[32]
PA/nxL	CHARMM/PCFF	~0.6-1.5	NR	Jump	~6	[33]
PA	GROMACS	~1.26	NR	Jump	~5-10	[34]
PA	NAMD	NR	NR	NA	~7	[35]
PA	DLPOLY/OPLS-AA	~1.3	~23	NA	~15	[36]
PA	GROMACS	NR	NR	NR	~24	[37]
PA	LAMMPS/GAFF	~1.28	~23	Jump	~5	[38]
PA	GROMACS	~1.35	NR	NR	~9	[39]
PA	LAMMPS	NR	~23	NR	~5-10	[40]
TMC/MPD	Experiment (mLBL)	NR	~23	NA	~5-80	[41]
PA	Experiment (mLBL)	NA	NA	NA	~1-25	[11]
PA	Experiment (IP)	NA	NA	NA	~1-15	[42]
PA	Experiment (IP)	NR	NR	NA	~6-20	[43]
PA	Experiment (IP)	NR	NR	NA	~5-33	[44]
PA	Experiment (mLBL)	NR	~15	NA	~2-100	[12]
PA	Experiment (IP)	NR	NR	NR	~20-80	[15]
PA	Experiment (IP)	NR	NR	NR	~10	[45]
PA	Experiment (IP)	NR	NR	NR	~6-16	[9]

NAMD (Not Another Molecular Dynamics Program) is a parallel MD code for simulating large biomolecular systems; GAFF is the generalized Amber force field, describing the interatomic interactions; CVFF is the consistent-valence forcefield, describing the interatomic interactions; CHARMM (Chemistry at Harvard Macromolecular Mechanics) is the name of widely used force fields, and the name for MD simulations software package related to them; PCFF (polymer consistent force field) is a member of the consistent family of second-generation force fields; DLPOLY is a classical MD simulation package developed at Daresbury Laboratory by W. Smith, T.R. Forester, and I.T. Todorov; Cerius2 is a molecular package for MD simulation; OPLS (Optimized Potentials for Liquid Simulations)-AA (all-atom) is all-atom-optimized potentials for liquid and organic molecule simulations; GROMACS (GROningen MAchine for Chemical Simulations) is an MD package mainly for simulating proteins, lipids, and nucleic acids. LAMMPS (Large-scale Atomic/Molecular Massively Parallel Simulator) is a classical MD package for materials modeling.

[a] Jump = Diffusion by jumping or hopping from one pore to another.

[b] Smooth = Diffusion is not monitored over a long MD simulation time.
[c] NR = Not reported or not calculated.
[d] NA = Not available.

MD simulations have become a more mature means of understanding the water treatment process and dynamic behavior through various membranes [26, 32, 46, 47]. These investigations indicated that the MD technique can effectively reveal the transport feature of atomic-scale water and ions under the condition of high-pressure reverse osmosis (HPRO) state within membranes [48]. To effectively manage brine water, HPRO potentially paves the way to enable more cost-effective and energy-efficient brine concentration. However, until now, HPRO is still fairly theoretical [48]. In most lab-scale RO experiments, the applied pressure ranges from about 0.2 to 1.7 MPa [49] and about 4.0 to 8.2 MPa [50] for brackish water and seawater, respectively. Recently, Wu et al. [51] investigated RO membrane embossing and compaction up to 20 MPa. But in practice, it is still challenging to demonstrate the water permeability at the experimental pressure for MD simulations within a few nanoseconds. Therefore, the applied pressures for conducting RO processes in simulations are much higher than that in experiments. To lower computational cost and statistical noise, pressures ranging from 30 to 150 MPa are employed to perform the HPRO processes for the common practice of MD simulations [35, 36, 52].

In this study, to build the structure-properties relationship for 3D-printed PA membranes, we systematically study how thicknesses act on the membrane's properties under HPRO *via* MD simulations. By mimicking experimental 3D-printing procedures, we first computationally generate PA membranes with thicknesses from 4.0 to 32.5 nm. Then, we connect water diffusion with membrane microstructure and water-accessible space based on equilibrium molecular dynamics (EMD) simulations. To deeply elaborate the structure-properties relationship with pure and brine water under HPRO (30 to 150 MPa), we performed non-equilibrium molecular dynamics (NEMD) simulations. After that, we evaluate membrane performance metrics, including structural features, pore size distribution (PSD), ions' dehydration, water diffusivity, water permeance and permeability, rejection and dynamic feature of ions, and transport mechanism. Eventually, we expect these investigations can deepen the understanding of thickness-dependent water and ion transport behaviors within 3D-printed membranes and advance the existing membranes for water desalination at the molecular level.

2. Computational Models and Methods

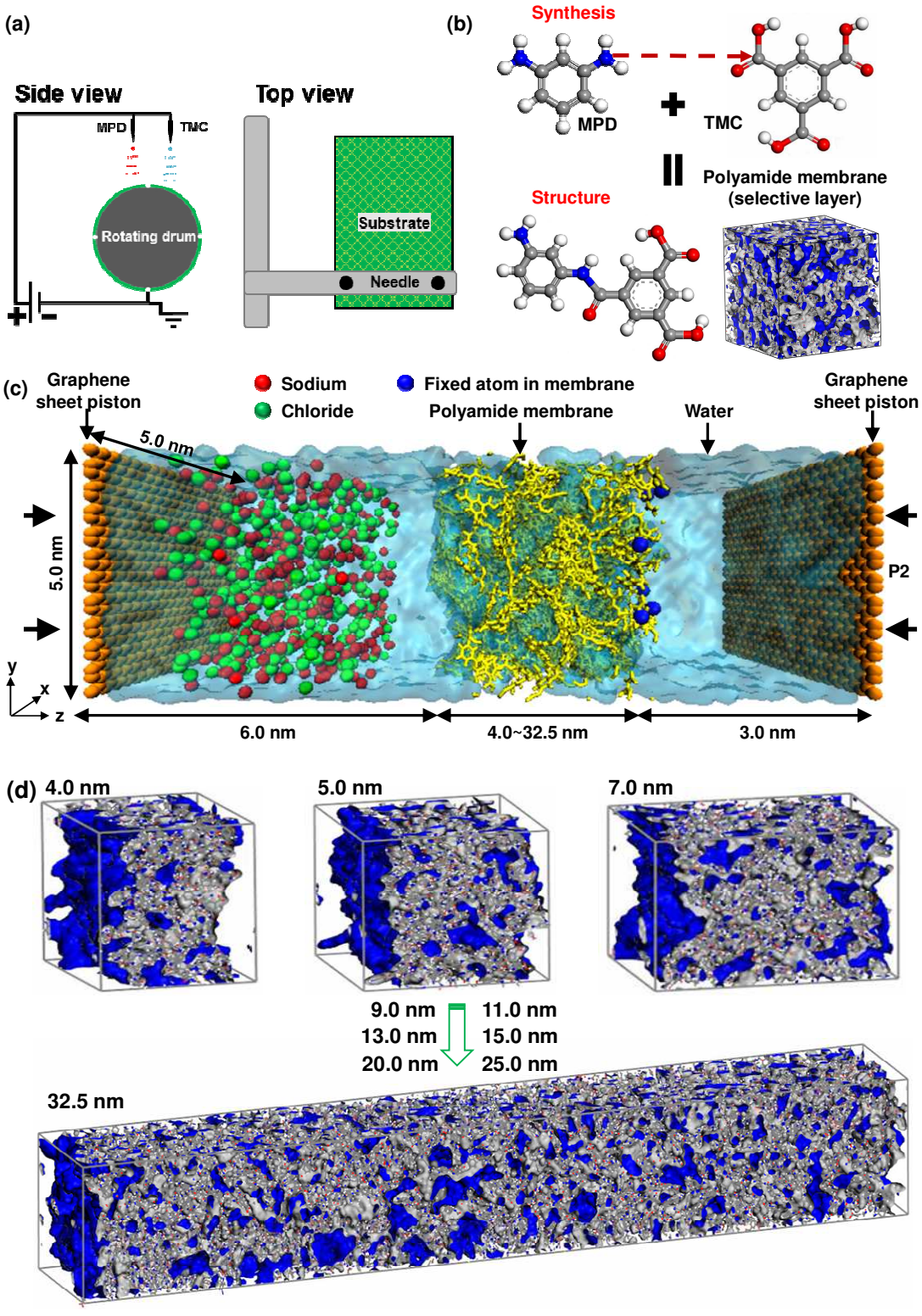

Fig. 1. (a) The experimental electrospray printing (3D-printing) procedure for manufacturing PA membranes [53]. (b) Cross-linking reaction for PA membranes, and the chemical structures corresponding to its two reactants, including MPD and TMC monomers. (c) Schematic for MD simulation setup visualized by VMD

[54]. The yellow and orange represent the PA membrane and graphene sheet pistons, respectively. The membrane thickness is changeable, ranging from 4 to 32.5 nm. Water is revealed as a light-blue transparent space. Green and red visualize salt ions, corresponding to chloride ions (Cl^-) and sodium ions (Na^+), respectively. The highlighted blue atoms within the PA membrane are locked to mimic the PA membrane contacted with polysulfone support in the experiment. During the simulation, P1 is exerted at the left side, and P2 (0.1 MPa corresponding to the standard atmosphere pressure) is applied to the right side. (d) Some representative configurations for PA membranes with different thicknesses, such as 4.0, 5.0, 7.0, 32.5 nm, are generated to mimic 3D-printing membranes.

2.1 Cross-linking process of the atomistic membrane models

Experimentally, as revealed in **Fig.1 (a),** electrospray printing is generally employed to deposit the 3D-printed PA membranes [53]. In a rotatable drum, one end attaches to the ground with another end attaching to two needles on the top. Each needle extrudes one monomer solution, such as TMC-hexane solution or MPD-water solution. In this way, MPD/TMC ratio is easily controlled at a required molar ratio during extrusion. As MPD-water and TMC-hexane solutions spray from the two needles, MPD and TMC monomers can deposit onto the support surface and conduct the random reaction. This unique method allows for unprecedented control over MPD/TMC ratio and more uniform reactivity compared to the traditional IP. Next, the printing process keeps on being conducted until the desired membrane thickness enables. Focusing on the manufacturing process, it is obvious that the 3D-printing also involves IP. Even so, our previous studies have elaborated that PA membranes' microstructure, permeability, and selectivity can reveal the essential differences between different manufacturing methods [13]. The 3D-printing techniques can provide more homogeneous reaction sites. Here, we would like to computationally reveal such unique features in 3D-printed PA membranes.

Computationally, the multi-step cross-linking reaction approach is employed to simulate the experimental 3D-printing procedure to generate highly cross-linked PA membranes [53]. As exhibited in **Fig. 1(b)**, considering the 5 nm-thick PA membrane (3:2 MPD/TMC ratio and 90% CD), reactive atoms (nitrogen (N) and carbon (C) atoms in carboxyl groups) are denoted on MPD and TMC monomers, respectively. Employing 1.30 g cm^{-3} as a target density, TMC (200) and MPD (300) monomers are randomly blended into a 3D-periodic cell with a lateral size of 5.0 × 5.0 nm. There are 600 available reaction sites in the system. Then, geometry optimization followed by 6 annealing cycles is carried out. Periodic boundary conditions (PBCs) are applied to the lateral directions (*x* and *y*), and a vacuum is applied to the *z* direction. Next, starting from an initial cutoff distance of 0.45 nm, cross-linking reaction is carried out in the canonical ensemble (NVT). Virtual springs are developed between the reactive sites within the cutoff

distance during the reactive process. These reacted atoms can be brought together under the action of the pulling springs by performing energy minimization and geometry optimization. When the distance of two reacted atoms is less than 0.15 nm, new cross-linked bonds (named C-N) are formed. The polymer network then continues to be relaxed to optimize the current configuration for 500 ps within the isothermal–isobaric (NPT) ensemble. Afterward, the reaction further proceeds to be carried out with an incremental 0.05 nm cutoff until the target CD (*e.g.*, 90%) is achieved. The CD is calculated at each reaction step by $\mathrm{CD}\,(\%) = \frac{\text{number of produced C}-\text{N bonds}}{\text{number of available C}-\text{N bonds}} \times 100$. When the target CD is achieved, the reaction process is terminated and bonds are prevented from further breaking/forming, a cross-linked PA membrane is eventually generated [55]. More technical details are given in our previous studies [6, 56].

During the experimental process of membrane fabrication, solvent molecules enter the solutions [57]. Thus, explicit solvent molecules should not have an intensive effect on the resulting PA membranes' properties. Instead, the additional interactions (*e.g.*, membranes and solvents, solvents itself) can reduce the monomer's diffusion speed, resulting in a retarded reaction process and raising the computational cost [58]. Therefore, the reaction process was conducted in a vacuum without any solvents. To maintain the system's charge neutrality principle, atomic charges are automatically modified in each reaction step by updating the force field parameters. Geometry optimization followed by 40 cycles for annealing system is further enforced to the produced membrane, and then the relaxed membrane is employed to perform the following simulations.

2.2 Hydration and desalination process for PA membranes

In order to match the 23 wt% water content in the membrane [59], PA membranes were driven to full hydration using EMD simulations through the physical interactions of water and membrane. Before conducting the hydration process, the graphene sheet with a cross-sectional area of 5 × 5 nm^2 is placed at both the feed and permeated side to restrain the reservoir. The two sheets keep 6 nm (left) and 3 nm (right) away from the middle membrane, respectively. After that, employing 1.0 g cm^{-3} (water density) as a basic density, water is randomly inserted into the system's water-accessible free space. Eventually, the generated structure was relaxed within the NVT ensemble over a long enough time to obtain the fully hydrated PA membranes [60]. As plotted in **Fig. 1(c)**, the desalination system is produced by adding some ions into the left reservoir (feed side) of the full hydration membrane. The employed salinity (feed side)

approaches that of concentrated brine (~4 M NaCl) [61], and the right reservoir (permeated side) is filled with pure water. After that, a long relaxation time is implemented within the NVT ensemble to relax the updated system and obtain the full equilibrium desalination system. Details related to MD simulations are described as follows.

2.3 Membrane systems for MD simulations

This study mainly focuses on how thickness affects membranes' properties. Other structural factors, such as MPD/TMC ratio and DC, are fixed at 3.0:2.0 and 90%, respectively, for PA membranes with different thicknesses. Then, ten PA membranes with different thicknesses were prepared, including 4, 5, 7, 9, 11, 13, 15, 20, 25, and 32.5 nm. As shown in **Fig. 1(d)**, six representative PA membranes are generated based on the cross-linking process aforementioned. Concerning a 5 nm PA membrane, the system has 200 TMC and 300 MPD, corresponding to the 3:2 MPD/TMC ratio. Then, these equilibrated membranes are employed to run HP RO simulations after graphene pistons, water molecules, and salt ions are assembled together.

2.4 HP water desalination via NEMD simulations

As presented in **Fig. 1(c)**, a model setup for all-atom NEMD simulations to investigate water and ion's dynamic features. For example, in a 5 nm PA membrane, the initial model is constructed by a cuboid box having a cross-sectional area of 5×5 nm^2 in the x-y plane and a length of 14 nm in the z-direction. At the position of $z = 0$ nm and $z = 14$ nm, two pistons are placed here. The PA membrane is initially located at $z = 6$~11 nm. Water molecules or ions are then added to the cuboid box. The inserted water molecule number corresponds to its density. Some salt ions (4M) are added to the left side ($0 < z < 6$ nm). Those randomly chosen membrane atoms colored by blue are fixed to simulate the surface contact with polysulfone support. Previous works indicated that these fastened atoms might slightly affect the flux but should have no influence on the water diffusion mechanism [17]. PBCs are only imposed on both x and y directions.

Interaction potentials associated with water molecules, ions, graphene, and membranes are calculated by polymer consistent force field (named PCFF) [62-64]. PCFF has been extensively applied to characterize organic compounds' mechanical properties, cohesive energies, elastic constants, etc. Atomic non-bonded interactions, including Coulomb and LJ potentials, are described as:

$$U_{\text{nonbonded}} = C\frac{q_i q_j}{\varepsilon r_{ij}} + \varepsilon_{ij}\left[2\left(\frac{\sigma_{ij}}{r_{ij}}\right)^9 - 3\left(\frac{\sigma_{ij}}{r_{ij}}\right)^6\right] \quad (1)$$

where C denotes the conversion factor, ε defines the dielectric constant, r_{ij} is the interatomic distance, ε_{ij} denotes the interatomic potential well depth, σ_{ij} is the interatomic distance where the potential obtains the minimum value, and q_i and q_j are respectively charges of atoms i and j. The interaction potentials among different types of atoms are described based on the six-power combination criteria [65]: $\sigma_{ij} = \left(\sigma_{ii}^6 + \sigma_{jj}^6\right)^{\frac{1}{6}}/2^{\frac{1}{6}}$ and $\varepsilon_{ij} = \sqrt{\varepsilon_i \varepsilon_j}\,(2r_{ii}^3 r_{jj}^3)/(r_{ii}^6 + r_{jj}^6)$. Interactions for long-range electrostatic are counted by employing the Particle–particle-particle–mesh (PPPM) algorithm (10^{-4} for force tolerance).

The LAMMPS simulation package is adopted to run all calculations [66]. 1.0 fs is chosen as the simulation time step. The integration method is based on the velocity-Verlet algorithm. During the equilibrium process, energy minimization is first implemented to avoid interatomic overlaps. Then, 0.1 MPa is imposed on two pistons. EMD simulations over 20 ns are carried out (within NVT ensemble at 300 K), ensuring PA membranes and solutions to enable full hydration or desalination. Performance metrics including diffusion coefficient, membrane density, and microstructure are monitored during the EMD simulation process.

Using the obtained equilibrium configurations from EMD simulations, NEMD simulations are conducted for both pure and brine water. A 0.1 MPa pressure first continues to implement on the two pistons. EMD simulations continue to be performed for further equilibrating the solutions and membrane over 2 ns (at 300 K and NVT ensemble). After that, an HP drop (ΔP = 30, 60, 90, 120, or 150 MPa) is exerted on the left side, and the pressure acting on the right piston is maintained at 0.1 MPa. NEMD simulations are carried out over a long simulation time (at 300 K and NVT ensemble). Here, a simulation assumption is water molecules' transport time linearly increases with the increasing membrane thickness. Thus, when the thickness raises from 4 nm to 32.5 nm, the production time used for NEMD simulation increases from 30 to 180 ns. Besides, the molecules' velocity is initialized using Gaussian distribution with a specific temperature of 300 K. Nosé-Hoover thermostat [67, 68] is applied to keep the temperature around 300 K. Performance metrics including permeance, flux, and rejection, microstructure, ions' dynamic behaviors, and water-accessible free space are monitored for NEMD simulations.

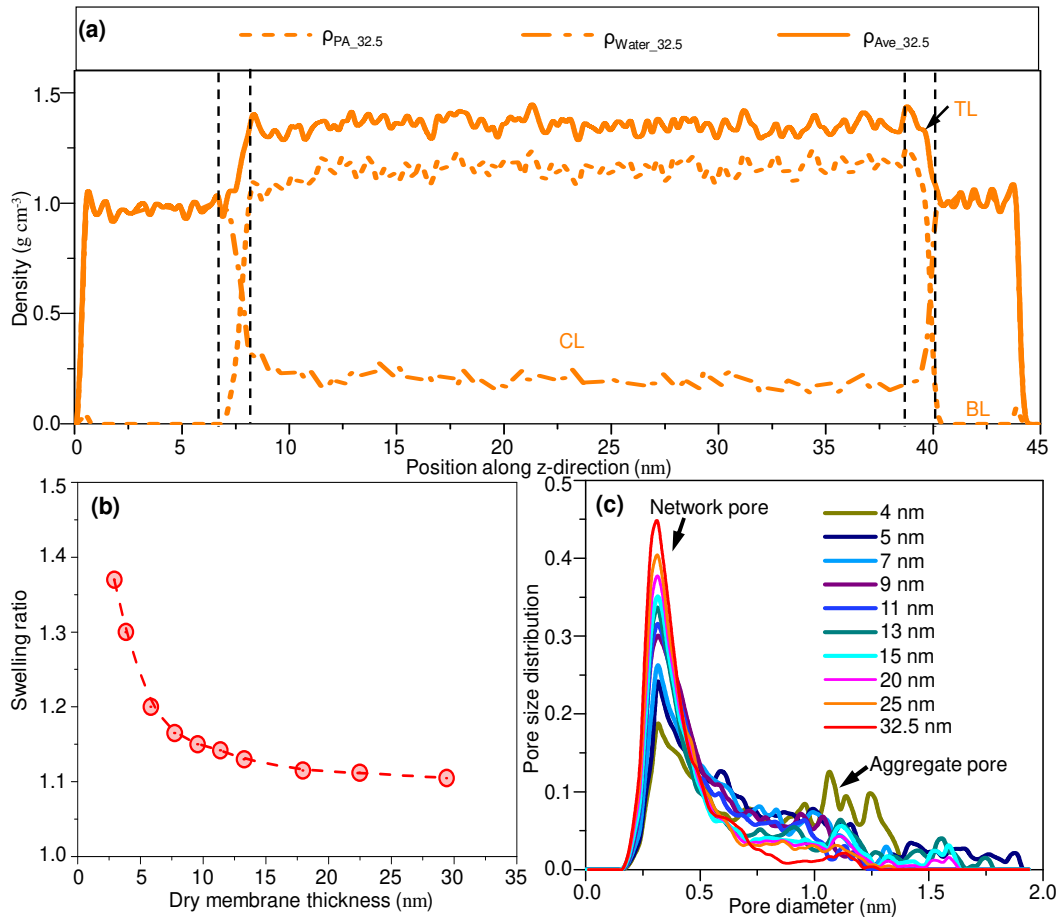

Fig. 2. (a) Density distributions in pure water for hydrated PA membranes and their two compositions (membrane and water). The solid lines are hydrated PA membranes, the dashed lines denote the PA membranes, and the dotted lines represent water. For clarity, only one membrane with a thickness of 32.5 nm is presented. (b) The relationship between membrane swelling ratio and dry membrane thickness. The red dashed line denotes the fitting curve. (c) PSD for membranes with thicknesses changing from 4.0 to 32.5 nm.

3. Results and Discussion

3.1 Atomic-scale structure feature for PA membranes with various thicknesses

To explore how thicknesses affect PA membrane's structural properties, we analyzed the swelling ratio, the density distributions for the hydrated membranes as well as their two components (MPD and TMC monomers) and PSD based on EMD simulations. As described in section 2.5, all the PA membranes use the same MPD/TMC ratio and DC. With such setups, the membrane thickness is isolated as the only factor responsible for the changes observed in the membrane's properties. Eventually, the atomic compositions (molar percentage) of carboxyl groups (-COOH), nitrogen (N), carbon (C), and oxygen (O in carbonyl groups), and were found to be about 3.70%, 12.35%, 72.84%, and 11.11%, respectively, for all membranes. These

calculated atomic compositions match well with the measurements reported by Coronell et al. [69]. The calculated PA membranes' densities are close to 1.26-1.27 g cm^{-3}, being also consistent with other experimental measurements (1.22-1.28 g cm^{-3}) [70], and computational simulations (1.25 g cm^{-3}) [38, 40, 71].

Next, the simulation system along the *z*-direction is divided into several slabs uniformly at 0.2 nm intervals. Then, their density distributions are analyzed based on the divided slab volume and the total atomic mass within each slab. Taking the thicknesses of 4.0, 15.0, and 32.5 nm as examples, **Fig. 2(a) and Fig. S1** plots the density distributions of full hydration PA membranes, water, and PA membranes. These profiles indicate each system can be roughly separated into three regions. For example, for the 15 nm-thick PA layer, the bulk layer (BL) corresponds to the bulk water, *i.e.*, located at z = 1 ~ 7 nm (feed side) and z = 22.5 ~ 25.5 nm (permeated side). The transition layer (TL) is between the dense membrane and bulk water, which is the lower-density region, *i.e.*, located at z = 7 ~ 8 nm (feed side) and z = 21.5 ~ 22.5 nm (permeated side). The low-density membrane is due to the fact that those uncompleted reacted monomers can move freely around the membrane surface because of membrane-water interactions. The confined layer (CL) is the dense polymer film, i.e., between z = 8.0 ~ 21.5 nm.

Notably, the three regions (CL, TL, and BL) for PA membranes are distinguished using density distribution of the z direction. BL is where the calculated density is close to 0.99 g cm^{-3}. TL is the region from the boundary of the membranes owning the smallest water density to the location of the membranes possessing 90% water density. CL is the region where membranes has the smallest water density. The definition related to the three regions as follows is the same as here. The water density of BL is calculated to be about 0.99 g cm^{-3} for PA membranes with different thicknesses, which is in good agreement with water density at 300 K [72]. The hydrated PA layer's density in the CL is found to be about 1.36 g cm^{-3}, which is consistent with experimental measurements (1.32 ± 0.1 g cm^{-3}) of the common FT-30 membranes [16, 73, 74].

Importantly, we explore the relationship between the swelling ratio and dry membrane thickness. Here, the swelling ratio is defined as the ratio of thickness at the hydration state to the thickness at the dry state. As shown in **Fig. 2b**, the membranes' swelling ratio decreases nonlinearly as the thickness increases, which indicates that thicker membranes resist swelling even when fully hydrated. As the thickness increases, the calculated PA membranes' swelling ratio shows a consistent trend with that obtained by experiment and theortical model [12, 75]. It

is worth note that the calculated swelling ratio for membrane with the same thickness is slightly lower than the measurements because of the different manufacturing methods. In addition, MD simulations offer an easy path to uncovering the membrane's PSD. Here, PSD curves are employed to describe the microstructure characteristics of PA membranes and quantify their pore space. PSD curves are calculated using PoreBlazer [76]. When a solvating molecule interacts with polar atoms, previous studies indicate that its size should be better described by its Coulombic diameter [77]. Many polar groups, such as –C=O, –NH, and =COOH, are naturally present in PA membranes. Thus, a 0.28 nm diameter probe corresponding to the Coulombic diameter of the water molecule is adopted to analyze membrane's PSD. Based on EMD simulations over 20 ns, the last ten frames are selected as membrane configurations to analyze their PSD. The resulting PSD curves are calculated by averaging these ten configurations.

Fig. 2(c) displays the resulting PSD profiles of PA membranes with various thicknesses. Videos for membrane microstructures after 20 ns production time under EMD simulations are provided as Supplementary Material (**V1-V4**) to clearly reveal their PSDs. PA membranes with different thicknesses have significantly different PSD, and PSD is more homogeneous as the thickness increases. When the thickness is below 5 nm, two types of pores are identified (i.e., network and aggregate pores [78]), which appear in the range of 0.2-1.0 nm and 1.0-1.5 nm, respectively. Instead, PA membranes with thicknesses larger than 5 nm only have network pores. Notably, those network pores mainly represent small free spaces surrounded by accumulation polymer segments, which originate from the cross-linked network among those reacted monomers. Aggregate pores are some large chain-to-chain spaces, which contain network pores and unreactive monomer fragments. As the thickness increases from 4 to 32.5 nm, on one side, the PSD becomes more uniform and pore distribution is more homogeneous; on the other side, the pore diameter corresponding to the PSD's peak stays the same, about 3.125 Å. These results suggest that a PA membrane's PSD may be modulated by tuning the membrane thickness.

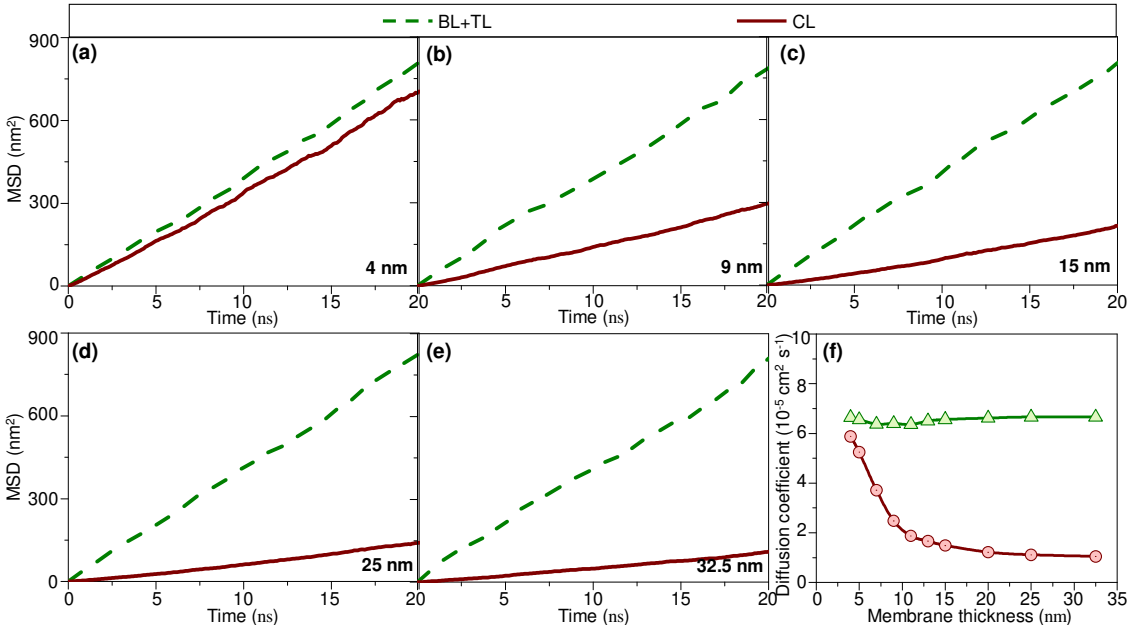

Fig. 3. MSD curves of water molecules in BL+TL, and CL for PA membranes having the thicknesses of (a) 4.0, (b) 9, (c) 15, (d) 25, and (e) 32.5 nm during the simulation time over 20 ns. (f) Water diffusion coefficient in BL, TL, and CL for PA membranes with thicknesses ranging from 4.0 nm to 32.5 nm.

3.2 Effect of thickness on water diffusion in PA membranes

Water diffusivity is an important metric to describe the dynamic behavior of water molecules as they transport within PA membranes [79]. For the PA-water system, in general, water molecules' mean squared displacement (MSD) scales linearly with the increasing simulation time, and its diffusion coefficient (D) is expressed as [80, 81]: $D = \lim_{t\to\infty} \langle |d(t) - d(0)|^2 \rangle / 6t$. Here, $\langle \blacksquare \rangle$ denotes the ensemble average, t is the simulation time, $d(0)$ and $d(t)$ represent water molecules' position at time 0 and t, respectively. Notably, the water molecules in the BL or TL region can diffuse into the TL or BL region, respectively. However, water molecules in both BL and TL regions are rarely admitted to the CL region. Hence, BL and TL regions are considered together to analyze the MSD. After the BL, TL, and CL are identified, the MSD and D in BL+TL and CL regions can be analyzed. **Fig. 3**(a-e) plots the water molecules' MSD in BL+TL, and CL over 20 ns for PA membranes with thicknesses varying from 4.0 to 32.5 nm. On the one hand, for each PA membrane, MSD always increases linearly with the simulation time. MSD in BL+TL is far greater than that in the CL. On the other hand, PA membranes with different thicknesses show almost identical MSD in the BL+TL. However, MSD in the CL decreases dramatically with increasing membrane thickness.

By fitting MSD curves in **Fig. 3**(a-e), water molecules' D in BL+TL, and CL for PA

membranes with thicknesses changing from 4.0 to 32.5 nm are presented in **Fig. 3**(f). results indicated that water diffusivities throughout the BL are slightly larger than in the TL but more extensive than that in CL for the same membrane thickness. Membranes with different thicknesses almost have the same diffusion coefficients D in BL+TL. **Fig. 3**(f) indicates bulk water's diffusivity is about 6.49×10^{-5} - 6.85×10^{-5} $cm^2\ s^{-1}$, which almost gives the same magnitude as the previously calculated result, about 5.1×10^{-5} $cm^2\ s^{-1}$ [71]. However, D in CL decreases nonlinearly with increasing membrane thickness, induced by the narrowing of PSD. These investigations illustrate water molecules diffuse the easiest in BL+TL, and slowest in the CL. Likewise, the water's diffusivity of CL for membrane thickness exceeding 15.0 nm is about 1.0 × 10-5 $cm^2\ s^{-1}$, which almost shows the same magnitude as the previous studies, about 2.5 × 10-6 - 2×10^{-5} $cm^2\ s^{-1}$ [82]. Membranes with a thickness of less than 15.0 nm give their distinct microstructures (**Fig.2c**), which can lead to slower water transport in CL with increasing thickness. However, when the thickness is larger than 20.0 nm, membranes show similar resistance to water transport due to their similar microstructures (**Fig.2c**).

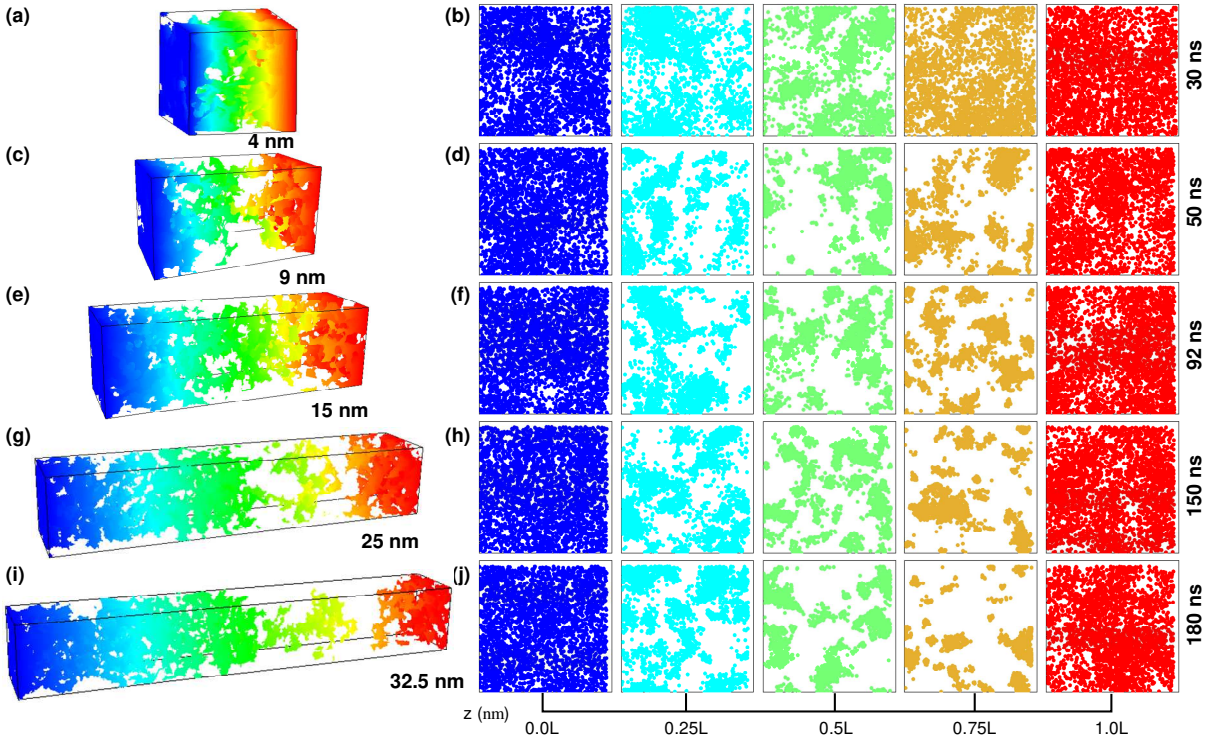

Fig. 4. The water-usable free space for PA membrane having a thickness of (a) 4 nm over 30 ns, (c) 9 nm over 50 ns, (e) 15 nm over 92 ns, (g) 25 nm over 150 ns, and (i) 32.5 nm over 180 ns at the full hydration state. The gradient color denotes a 1.0 Å-thick plane along the z direction. The cumulated water-available space for PA membranes with thicknesses of (b) 4 nm over 30 ns, (d) 9 nm over 50 ns, (f) 15 nm over 92 ns, (h) 25 nm over 150 ns, and (j) 32.5 nm over 180 ns at z = 0.00L, 0.25L, 0.50L, 0.75L, and 1.00L. Note that L

is the membrane thickness within the z-direction and the color denotes the z-position.

3.3 Effect of thickness on the dynamic behavior of transported water molecules

PSD curves in **Fig. 2(c)** demonstrate that PA membranes could possess distinct PSD's for different membrane thicknesses. Previous studies also indicated that water transport rates correlate with membrane pore distribution. To better understand how water molecules permeate PA membranes, the pore space is further quantified using the water-usable free space's continuous. Similar to PSD analysis, a 0.28 nm diameter probe is selected to analyze the water-usable free space within PA membranes. **Fig. 4(a, c, e, g, i)** plots the water-usable space for PA membranes with various thicknesses over their production time at 150 MPa. Here, we only evaluated PA membranes with the thickness of 4, 9, 15, 20, and 32.5 nm. Videos of the water-available free space at 150 MPa corresponding to **Fig. 4(a, c, e, g, i)** are provided by Supplementary Material (**V5-V8**) to demonstrate the water-usable space's connectivity. The whole thickness region is represented by color varying from blue to red. The colored space reveals the water-usable space where water resides in the membrane. Obviously, the water-accessible space has significant differences as the membrane thickness changes. The thicker membranes only have the locally connected water-accessible space, while the thinnest membrane (4 nm) shows the percolated connectivity in the water-usable space.

In addition, we analyzed the PA membrane's dynamic pore sizes during the water diffusion process to further describe the correlation between water-usable space and the diffusion mechanism. The dynamic pores are the result of intermolecular interactions, e.g., membrane-water molecules' collisions and vibrations, further represented by the accumulated water-available space over enough long production simulations. **Fig. 4(b, d, f, h, j)** displays the water-usable space cumulated over their production time at five membrane locations, e.g., at z = 0, 0.25L, 0.5L, 0.75L, and L (L is membrane thickness). Results indicate that the thinner membranes enable more water molecules to travel throughout the membranes.

Moreover, previous studies have elaborated that the permeated water molecules are directly associated with the permeability coefficient, pressure, and membrane thickness [52]. The thicker membranes give less water-accessible space, resulting in less water passing through the membranes. As shown in **Fig. 4(a-j),** when the membrane thickness is larger than 5.0 nm, water molecules are unable to develop the connected channels throughout the membrane. In other words, the temporary open-and-close cavities govern the water diffusion within the

membranes, which only allow water to pass through the membranes by jumping. However, when the membrane thickness is below 5.0 nm, water can pass through the membrane in two distinct ways. One is the connected water channels, and the other is the jumping through the dynamic open-and-close pores. It is important to note that the percolated water-accessible free volume distribution at a single moment and the accumulated water-accessible space over their production time at five locations cannot accurately depict their PSDs. The former only describes the instantaneous water distribution behavior due to the dynamic variation of pores under high pressure, while the latter only shows the impact of membrane thickness on water transport efficiency. **Fig. 2c** presents the PSD of PA membranes with different thicknesses prior to applying pressure. The PSDs after pressure can be found in **Sect. 3.6.** Since the PSDs are uniform, the subsequent analysis of thickness' effect on membrane properties should remain the same, no matter which membrane side is used as the feed region.

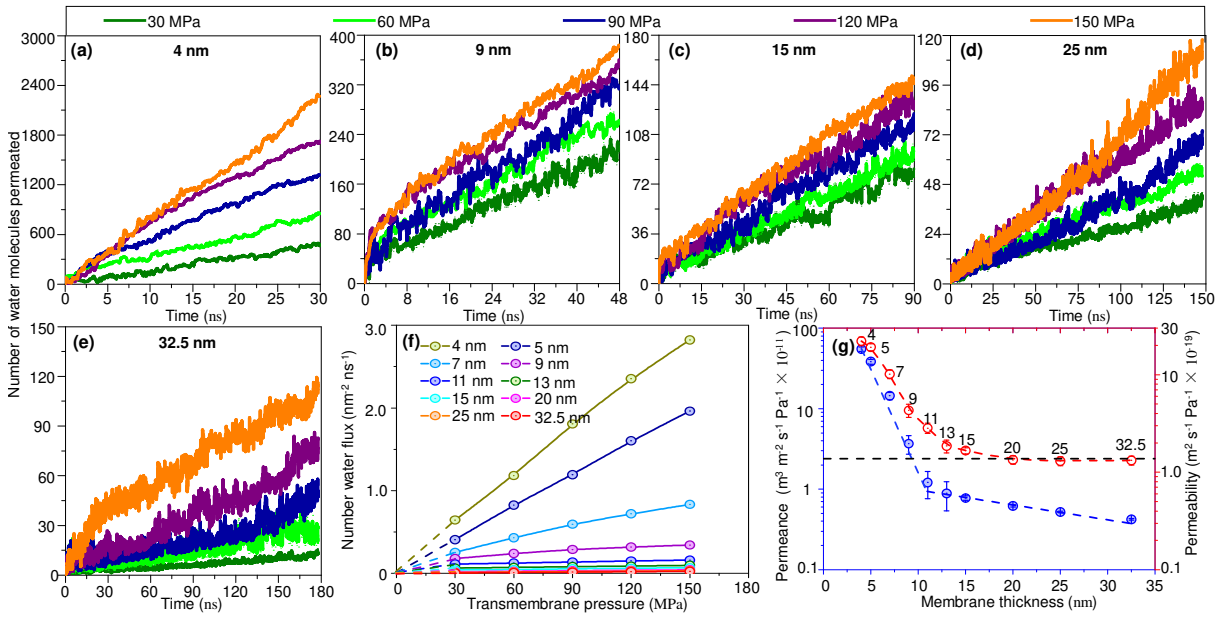

Fig. 5. Effect of thickness on pressure-driven pure water transport across PA membranes. The membrane thickness varies from 4.0 to 32.5 nm, and the pressure changes from 30 to 150 MPa. (a, b, c, d, and e) The variation between the passed water molecules and the production time at various pressures. For clarity, only five membrane thicknesses are plotted, including 4, 9, 15, 25, and 32.5 nm. (f) Relationship between water flux and the imposed pressures for PA membranes with different thicknesses. (g) Correlation between water permeance (blur color) and thickness, and water permeability (red color) and thickness. The dashed lines (blue and red) denote the fitting curves.

3.4 Effect of membrane thickness on pure water transport at HP

By comparing some key metrics with other measurements and simulations under the same condition [52, 78, 83, 84], such as PSDs, membrane density, water content, and water

flux, our previous studies demonstrate that our current models and time scales of NEMD simulations are reasonable [6, 85]. In order to explore how membrane thicknesses affect the pure water transport at HP, NEMD simulations are conducted for PA membranes with different thicknesses at 30, 60, 90, 120 and 150 MPa over a long enough simulation time. Performance metrics, including the passed water molecules, water flux and permeability, are calculated to evaluate the PA membrane's properties. **Fig. 5(a-e)** and **Fig. S2 (a-e)** show the variation between the transported water molecules and the growing production time scale for PA membranes with thicknesses ranging from 4.0 to 32.5 nm at 30 to 150 MPa. In the first 5 ns, a rapid increase in the transported water molecules shows some water molecules can be quickly extruded into the right reservoir because of the compacted membrane caused by HP RO. Afterward, the passed water molecules approximately increase linearly with the growing time for the PA membrane with a given thickness. Considering the same pressure condition, more water molecules can travel through the thinner membranes, echoing their pore features displayed in **Fig 2(c)** and the water-usable space presented in **Fig. 4(a-j)**.

Moreover, according to these curves' slope within the linear regime (**Fig. 5(a-e)** and **Fig. S2 (a-e)**) and the membrane's cross-sectional size, we further evaluate the water flux of these PA membranes. As plotted in **Fig. 5(f)**, we show the water flux versus the different pressures (30 to 150 MPa) for PA membranes with various thicknesses (4.0 to 32.5 nm) in the light of the transported water molecules (per unit area and time). On the one hand, following the increased pressure, the flux linearly increased almost for the PA membrane at a given thickness. On the other hand, as the thickness increases, the water flux dramatically decreases at the same pressure. In addition, we establish the relationship between water permeance and thickness, and between water permeability and thickness. By fitting the curves in **Fig. 5(f)**, we plot both water permeance and permeability versus membrane thickness, as given in **Fig. 5(g)**. Interestingly, water permeance proportionally decreases as the membrane thickness increases. Water permeability monotonically decreases with increasing thickness and has no statistically significant difference when the thickness exceeds 15.0 nm. Therefore, employing water permeability as the transport metric, these investigations indicate that 15.0 nm can be identified as the critical membrane thickness for efficient water transport.

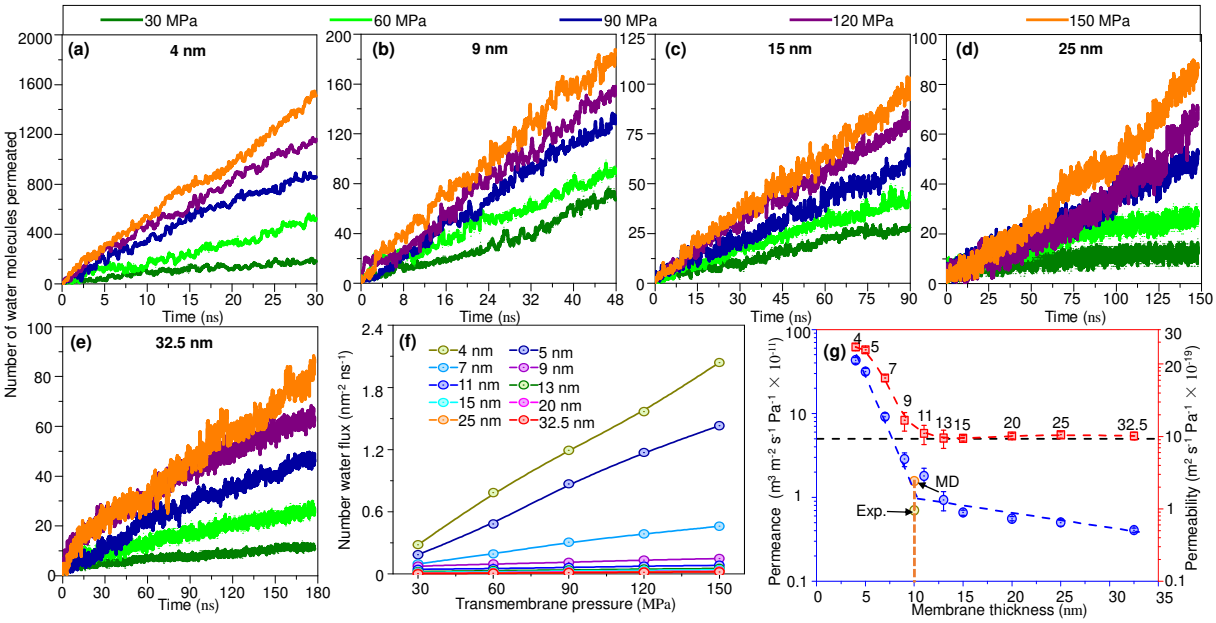

Fig. 6. Effect of thickness on brine water transport across PA membranes at HP. The membrane thickness varies from 4.0 to 32.5 nm, and the pressure changes from 30 to 150 MPa. (a, b, c, d, and e) The traveled water molecule number versus the production time at different HPs with brine water. For clarity, only five membrane thicknesses are given, including 4, 9, 15, 25, and 32.5 nm. (f) Correlation between water flux and transmembrane pressure for PA membranes with different thicknesses. (g) Water permeance (blue) and permeability (red) as a function of membrane thickness. The dashed lines (blue and red) denote the fitting curves. In comparison, we also calculate the water permeance at the salty of 2 g L^{-1}. The light green and orange respectively denote the experimental value and simulation.

3.5 Effect of thickness on brine water transport at HP

To understand the effect of thickness on water and salt ions' dynamic behaviors at HP RO, we track the traveled water molecules, water permeance, water flux and ion rejection. **Fig. 6(a-e)** and **Fig. S3 (a-e)** plot the relationships between traveled water molecules and the growing production time at HP for PA membranes with an increasing thickness from 4.0 to 32.5 nm. For brine, the passed water molecules have a linear increase as the production time increases and positively correlates with the increasing HP for the membrane with a specific thickness after 5 ns. However, the permeated water molecules are dramatically reduced at the same pressure as the membrane thickness increases, demonstrating the influences of membrane pore structure and diffusion path length given in **Fig 2(c)** and the water-accessible space presented in **Fig. 4(a-j).**

We also analyzed the water flux based on the membrane's lateral area and those curves' slope within the linear regime shown in **Fig. 6(a-e)** and **Fig. S3 (a-e)**. **Fig. 6(f)** gives the relations between water flux and transmembrane pressures for PA membranes with thickness changing from 4.0 to 32.5 nm in brine water. These investigations indicated that water flux is linear with the pressure for the membrane with a given thickness, and reduces nonlinearly with increasing

membrane thickness. Moreover, we further establish the corresponding relations between thickness and water permeance, and between thickness and water permeability by fitting these curves in **Fig. 6(f)**. **Fig. 6(g)** plots the water permeance and permeability versus thickness. Water permeance is presented as a propositional decrease as the thickness increases. However, water permeability shows an exponential reduction with increasing thickness, and falls to a certain threshold. It is worth mentioning that, although we use extremely high pressure in this study, we have applied the extrapolation method from previous molecular dynamics (MD) studies on high-pressure reverse osmosis (RO) membranes [26] to validate our simulations, which is a common practice in this field. Besides, other MD simulations indicate that high pressure is also effective for PA membrane as well [35-37]. However, it is important to note that the microscopic phenomena observed under extremely high-pressure conditions may not be representative of those under more realistic pressure conditions. In addition, by comparing with membrane properties in our NEMD simulations at high pressure, other investigations [48, 51] show the different phenomena for membrane property (water flux) at the realistic HPRO. The reason is that those used membrane materials are not PA RO membranes. Importantly, membrane properties have a strong dependence on membrane composition and pore distribution. Besides, for the same PA membranes, one recent investigation showed that membrane properties are almost linear with the increasing pressure at the realistic HPRO [86]. Similar to pure water, upon reaching the 15.0 nm thickness, water permeability is also constant for thicker PA membranes.

Beyond that, taking a 10 nm-thick membrane as an example, we also calculate the water permeance when the salt concentration is 2.0 g L^{-1}. The simulated water permeance is about 0.7 $\times$ 10^{-11} m^3 m^{-2} s^{-1} Pa^{-1} (red circle in **Fig. 6(g)**), which almost shows the same magnitude as the experimental measurement (0.41 $\times$ 10^{-11} m^3 m^{-2} s^{-1} Pa^{-1}) [42] (green circle in **Fig. 6(g)**). Compared with pure water transport in **Fig. 5(a-g)** and **Fig. S2 (a-e)**, the membrane with a given thickness has a lower water flux and water permeance with brine water. These findings suggest that both salt ions and membranes' thickness limit water transport. It is worth noting that salt ions limit water transport in a different physical way compared with the thickness effect. A more concentration of salt ions requires a greater hydraulic pressure to neutralize the osmotic pressure difference across membranes [87]. Likewise, using water permeability as the transport metric 15.0 nm can be identified as the critical thickness for efficient water transport.

Next, focusing on salt ions' dynamic features, we analyze their rejection by PA membranes with various thicknesses at various HP. **Fig. S4** plots the salt ions' rejection versus pressures for PA membranes with the thicknesses changing from 4.0 to 32.5 nm. Here, the salt ions' rejection is equal to one minus the percentage of the ions at the permeated side to the total ions within the system. The membrane with each thickness reveals a 100% rejection ratio, which suggests that membranes can totally hinder all salt ions over the simulation time. Note that the salt (NaCl) rejection by PA membranes in experiments is typically about 95~99% [15, 88], which is performed from hours to days. In contrast, our MD simulations are limited to hundreds of nanoseconds. Therefore, we do not observe any salt ions penetrating through PA membranes in these MD simulations over the simulation timescale.

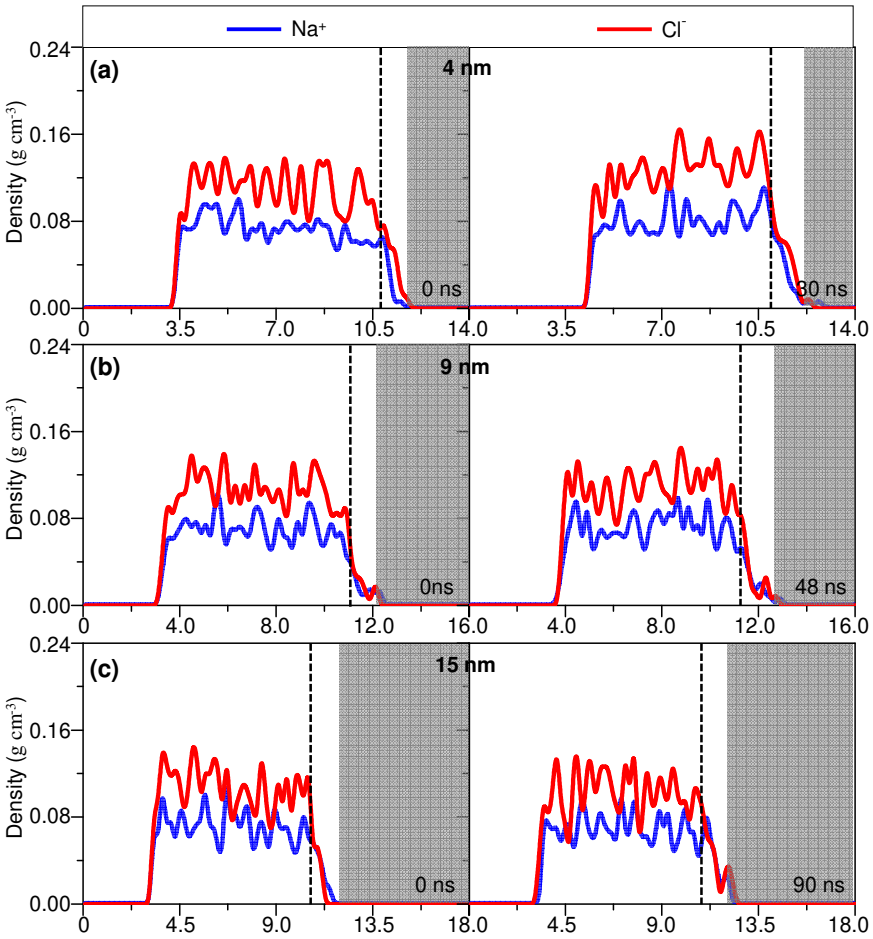

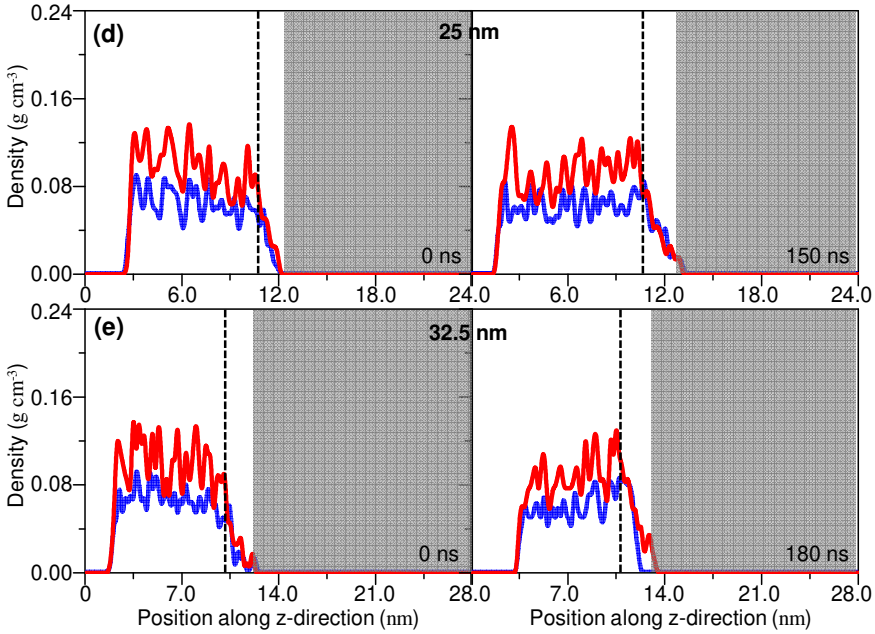

Fig. 7. Salt ions' density profiles for the PA membrane with a thickness of (a) 4, (b) 9, (c) 15, (d) 25 and (e) 32.5 nm along the z-direction before applying a pressure (0 ns, left side), and over the simulation time (from 30 to 180 ns, right side) after applying 150 MPa transmembrane pressure. Na^+ and Cl^- ions are represented by blue and red, respectively. The gray represents half of the CL and the dashed lines define the TL at feed side.

3.6 Effect of thickness on the dynamic features of salt ions and water molecules

To investigate the salt ions' dynamic behavior within PA membranes, we first calculate the density distribution of salt ions. **Fig. 7(a-e)** and **Fig. S5 (a-e)** plot salt ions' density profiles including Na^+ and Cl^- for PA membranes with the thickness of 4, 9, 15, 25 and 32.5 nm before the pressure is exerted (0 ns, left side), and over a long simulation time (from 30 to 180 ns, right side) after a 150 MPa acting on the left piston. Similarly, the membrane with a given thickness can be divided into three regions after applying a 150 MPa pressure. considering the 9 nm PA membrane, the shadow area denotes half of the dense membrane, i.e., between z = 12.4 to 16.0 nm. The dotted line denotes the left transition region, i.e., between z = 11.6 to 12.4 nm. The left dotted line represents the bulk water region. Before applying the pressure, salt ions reveal a similar density distribution for membranes with different thicknesses due to their ionic nature. For example, no ions exist in the position of water-graphene interface and the CL membrane region, and some ions accumulate in the TL due to their electrostatic interactions with the PA membrane. Such distribution is quite dissimilar to those investigations related to small organic solutes [26, 46, 89, 90]. After applying 150 MPa pressure and performing a long simulation, still, no salt ions reside at the interface region (water-graphene). More ions could gather at the TL region due to the HP. Some salt ions could enter the CL membrane region, particularly, in

the thinner membranes, while they still cannot pass through the membrane over the simulation time. These observations also indicate that PA membranes with various thicknesses can entirely reject the salt ions over the simulation time, corresponding to a 100% rejection ratio in **Fig. S4.**

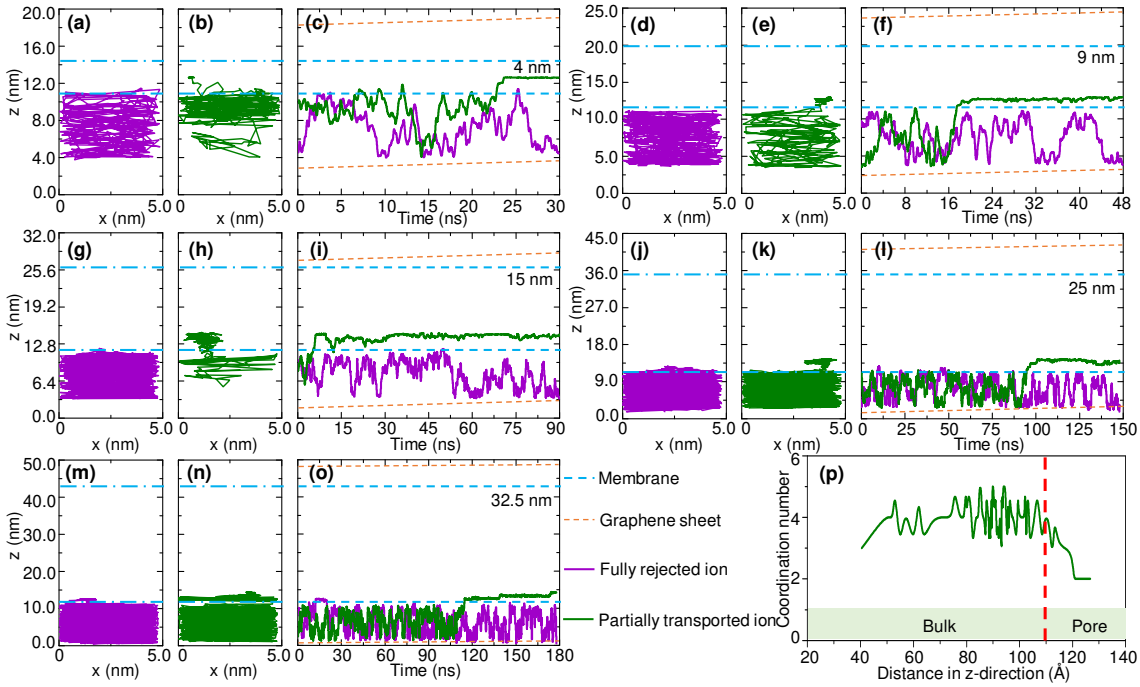

Fig. 8. Typical trajectories of salt ions interacting with the PA membrane owning a thickness of (a–c) 4 nm, (d–f) 9 nm, (g–i) 15 nm, (j–l) 25 nm, and (m-o) 32.5 nm when imposing a 150 MPa transmembrane pressure. The left represents an entirely rejected salt ion trajectory over the simulation time. The middle shows the trajectory of a traveled salt ion over the production time. The right shows the z-trajectory versus the increased production time for the two monitored ions. Cyan denotes the membrane position, and orange denotes the location of the graphene pistons. (p) Coordination number of the partially transported sodium ion versus the z-distance from bulk water into the pore space in the 4.0 nm membrane.

Next, based on NEMD simulations, we monitor the trajectories of some important ions in PA membranes with various thicknesses to understand their transport features at HP. **Fig. 8(a-c)**, **Fig. 8(d-f)**, **Fig. 8(g-i)**, **Fig. 8(j-l)**, and **Fig. 8(m-o)** plot the trajectories of the monitored ions within PA membranes with thicknesses of 4, 9, 15, 25, and 32.5 nm during the simulation time, respectively. The purple line in **Fig. 8(a, d, g, j, m)** represents the trajectory of an fully hindered salt ion. The trajectory of a salt ion traveling the furthest within the membrane is plotted as the green line in **Fig. 8(b, e, h, k, n)**. **Fig. 8(c, f, i, l, o)** plots the *z*-trajectories of two monitored ions versus the increasing production time. Significantly, the entirely hindered salt ions have a curvilinear trajectory back and forth within the bulk water region. However, after a long simulation time, a few ions diffuse into the confined membrane but still cannot pass through the

membrane, remaining at a particular location. In addition, we further plotted the relationship between coordination number and z-distance for the partially transported ion moving from the feed region (bulk water) into the pore space of the 4 nm-thick PA membrane. Here, the coordination number (water molecule number encompassing one ion) is calculated from the average water molecule number within the ion's hydrated radius. As exhibited in **Fig. 8p**, the result showed that water molecules were gradually detached from the hydration layer to permit salt ions to "squeeze" into the membrane pore space. Finally, The coordination number of the transported salt ion reduced from four to two as it traveled from bulk water into membrane pore space, indicating that the salt ion was partially dehydrated from its inner hydration layer (the loss of two water molecules).

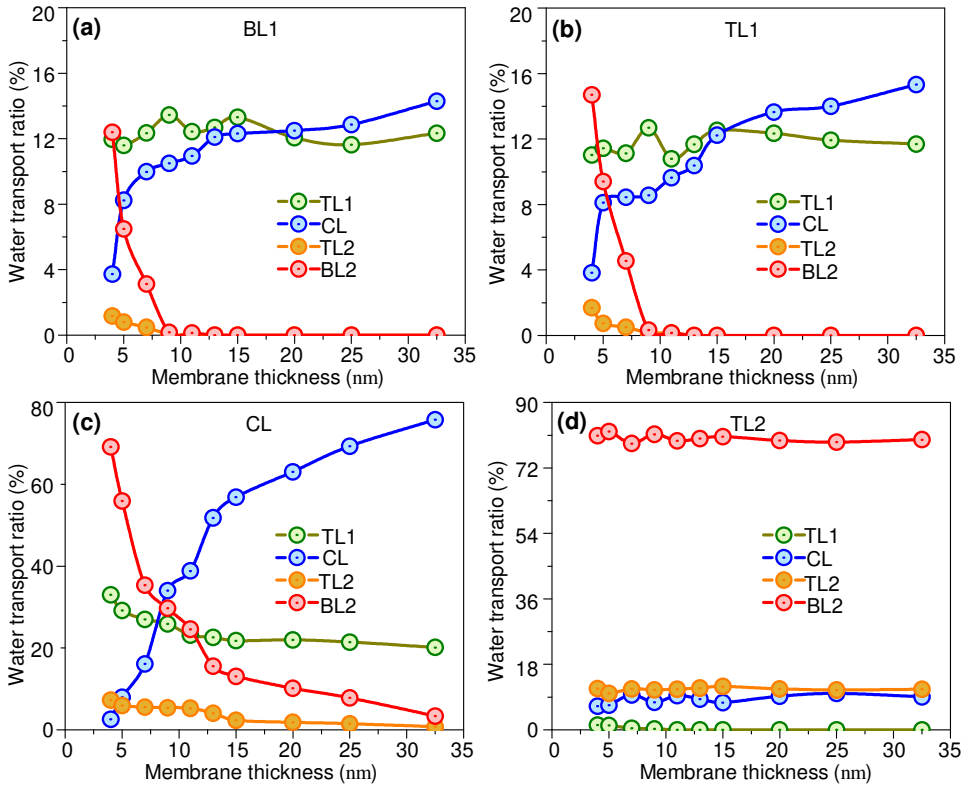

Fig. 9. Regional contribution ratio of (a) BL1, (b) TL1, (c) CL, and (d) TL2 as a function of membrane thickness for water transport.

We further analyze the regional contribution ratio for PA membranes with different thicknesses to understand water transport behavior. Considering a 15 nm-thick PA membrane, the equilibrium configuration is first obtained using EMD simulations over 20 ns. As plotted in **Fig. S6**, the density distribution of the system is then calculated using the last 1 ns configuration.

Next, based on the density profile shown in **Fig. S6**, the PA membranes can be divided into three regions, including TL (TL1 and TL2), CL, and BL (BL1 and BL2). In the beginning, we first mark the water molecules based on each divided region. Next, after performing a long simulation, those marked water molecules in one region could move into other regions. Then the number of those initially marked water molecules corresponding to each divided region is again reported. Therefore, The regional contribution ratio is counted using the percentage of final numbers to initial numbers for those marked water molecules in each region. Based on the NEMD simulations, the regional contribution rate of BL1, TL1, CL, and TL2 is plotted in **Fig. 9 (a-d)**, respectively. For example, **Fig. 9a** indicates how many water molecules located in BL1 could move into TL1, CL, TL2, and BL2 after a long simulation time. Evidently, as shown in **Fig. 9 (a-c)**, focusing on water molecules located in BL1, TL1, and CL at the beginning (t=0), water molecules are difficult to get into BL2 but easy to stay at CL as the thickness increases. In order words, more water molecules are allowed to diffuse through the thinner membranes and stayed at the confined layer (CL) for the thicker membranes over the simulation time. Meanwhile, membrane thickness shows no effect on water molecules in the transition region (TL1 and TL2). Besides, considering water molecules resided in CL or TL2 at the beginning, as plotted in **Fig. 9 (c-d**), it can be found that a small portion of water molecules reveal a back-streaming effect around the membrane at HP.

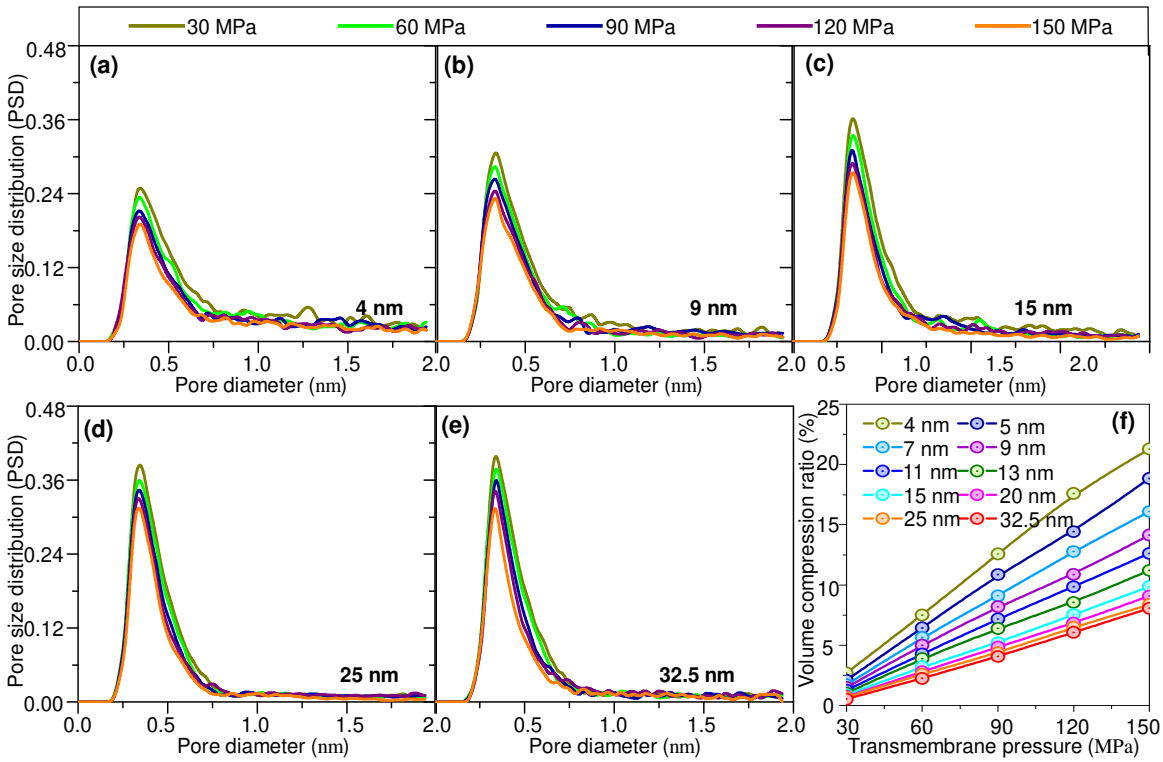

Fig. 10. PSD of PA membranes with the thickness of (a) 4, (b) 9, (c) 15, (d) 25, and (e) 32.5 nm at HP (30~150 MPa). (f) The compression ratio of membrane volume versus HP for PA membranes with different thicknesses.

3.6 Microstructure features for PA membranes with different thicknesses under HP

To illustrate how membrane thickness affects its microstructural characteristics at HP with brine water, we first calculate the PSD of PA membranes with different thicknesses. Likewise, using a 0.28 nm diameter probe, as shown in **Fig. 10(a-e)** and **Fig. S7 (a-e),** we plot the corresponding PSD for PA membranes with thicknesses ranging from 4.0 to 32.5 nm at HP (30~150 MPa). Results suggest that PA membranes with different thicknesses reveal distinct differences in PSD at HP. On one side, the PSD amplitude has a distinct reduction in the full pore diameter region for PA membranes with various thicknesses at HP. It indicates that the applied HP can result in membrane compaction. On the other side, as shown in **Fig. 10f,** we also calculate the volume compression ratio of PA membranes with different thicknesses at HP. Results indicate that the membrane compaction ratio decreases as thickness increases. Such reduction can be attributed to the increasing thickness and different microstructures (**Fig. 10(a-e)**). Our investigations with extremely high pressure, due to computational constraints, could provide reliable predictions for low-pressure water flux. The linear pure water flux-pressure curves, intersecting the vertical axis at the origin, support the reliability of these predictions.

These findings, related to intrinsic membrane properties, will aid experimental studies and facilitate molecular-level membrane design for water desalination.

4. Conclusion

This work systematically studied the molecular level structure-property relationships for 3D-printed PA RO membranes operating at high pressures. Specifically, we evaluated membrane density, cross-linking degree, diffusion coefficient, water flux, water permeance and permeability, salt rejection and local transport features in different regions throughout the membrane. These investigations are elaborated by analyzing water and salt ion dynamic behaviors.

Structurally, membranes with different thicknesses reveal some discernible patterns in PSD curves. First, the pore diameter corresponding to the PSD peak for membranes with different thicknesses is the same, about 3.125 Å. Second, as the membrane thickness increases, the fractional content of cross-linked network pores increases and the PSDs are more homogeneous. Third, the swelling ratio decreases nonlinearly with increasing thickness. Water diffusivity also decreases nonlinearly with increasing thickness. In pure and brine water, water flux and permeance proportionally decrease with increasing thickness. No statistically significant difference is observed for water permeability when the thickness exceeds 15.0 nm. Hence, 15 nm is considered a threshold thickness for the PA layer above which the molecular structure of the film remains consistent. At or below 5.0 nm, water transport occurs through continuously open and connected channels, whereas for thicker films it is dependent upon temporarily open-and-close pores. Membranes with various thicknesses can entirely reject all salt ions over the simulation time (10-100 nano-seconds), which is likely too short of a time to evaluate practical salt rejection.

Additionally, in brine water at HP, the PSD amplitude is lower, which suggests HP can result in membrane compaction and pore size/volume reduction. Importantly, thicker membranes resisted compaction. Here, all simulations are limited to a DC of 90%, an ideal 3.0:2.0 MPD/TMC ratio, and a timescale of tens to hundreds of nanoseconds. Exploring different CDs and MPD/TMC ratios over longer times could help better understand how to optimally design 3D-printed PA membranes to achieve the desired salt rejection.

Author Statement

Jinlong He: Validation, Conceptualization, Methodology, Software, Data curation, Visualization, Formal analysis, Writing – original draft. Tom Arbaugh, Danh Nguyen, and Weikang Xian: Conceptualization, Software, Methodology, Writing – review & editing. Eric M. V. Hoek and Jeffrey R McCutcheon: Methodology, Conceptualization, Project administration, Supervision, Funding acquisition. Ying Li: Methodology, Software, Conceptualization, Writing – review & editing, Funding acquisition, Supervision, Project administration.

Declaration of Competing Interest

Jeffrey McCutcheon is an equity owner of a faculty-affiliated company commercializing printing technology for membranes. The other authors state that there are no personal relationships or known competing financial interests that may appear to affect the work reported in this study.

Acknowledgements

Y.L., J.R.M, and E M.V. H would like to thank the support from the National Alliance for Water Innovation (NAWI), funded by the U.S. Department of Energy, Office of Energy Efficiency and Renewable Energy (EERE), Advanced Manufacturing Office, under Funding Opportunity Announcement Number DE-FOA-0001905. Y.L. gratefully acknowledges financial support from the U.S. National Science Foundation (CMMI-1762661, CMMI-1934829, and CAREER Award CMMI-2046751) and 3M's Non-Tenured Faculty Award. Any opinions, findings, conclusions, or recommendations expressed in this material are those of the authors and do not necessarily reflect the views of the U.S. National Science Foundation and Department of Energy. The research was performed using computational resources sponsored by the Department of Energy's Office of Energy Efficiency and Renewable Energy and located at the National Renewable Energy Laboratory (Eagle Computing System).

REFERENCE

[1] P.J.J. Alvarez, C.K. Chan, M. Elimelech, N.J. Halas, D. Villagrán, Emerging opportunities for nanotechnology to enhance water security, Nat. Nanotechnol., 13 (2018) 634-641.

[2] M. Elimelech, A. Phillip William, The Future of Seawater Desalination: Energy, Technology, and the Environment, Science, 333 (2011) 712-717.

[3] L.F. Greenlee, D.F. Lawler, B.D. Freeman, B. Marrot, P. Moulin, Reverse osmosis desalination: Water sources, technology, and today's challenges, Water Res., 43 (2009) 2317-2348.

[4] K.P. Lee, T.C. Arnot, D. Mattia, A review of reverse osmosis membrane materials for desalination—Development to date and future potential, J. Membr. Sci., 370 (2011) 1-22.

[5] J.G. Wijmans, R.W. Baker, The solution-diffusion model: a review, J. Membr. Sci., 107 (1995) 1-21.
[6] J. He, J. Yang, J.R. McCutcheon, Y. Li, Molecular insights into the structure-property relationships of 3D printed polyamide reverse-osmosis membrane for desalination, J. Membr. Sci., 658 (2022) 120731.
[7] S. Ling, Z. Qin, W. Huang, S. Cao, D.L. Kaplan, M.J. Buehler, Design and function of biomimetic multilayer water purification membranes, Sci. Adv., 3 e1601939.
[8] X. Peng, J. Jin, Y. Nakamura, T. Ohno, I. Ichinose, Ultrafast permeation of water through protein-based membranes, Nat. Nanotechnol., 4 (2009) 353-357.
[9] Z. Jiang, S. Karan, A. Livingston, Water Transport through Ultrathin Polyamide Nanofilms Used for Reverse Osmosis, Adv. Mater., 30 (2018) 1705973.
[10] H. Yan, X. Miao, J. Xu, G. Pan, Y. Zhang, Y. Shi, M. Guo, Y. Liu, The porous structure of the fully-aromatic polyamide film in reverse osmosis membranes, J. Membr. Sci., 475 (2015) 504-510.
[11] J.-E. Gu, S. Lee, C.M. Stafford, J.S. Lee, W. Choi, B.-Y. Kim, K.-Y. Baek, E.P. Chan, J.Y. Chung, J. Bang, J.-H. Lee, Molecular Layer-by-Layer Assembled Thin-Film Composite Membranes for Water Desalination, Adv. Mater., 25 (2013) 4778-4782.
[12] W.D. Mulhearn, V.P. Oleshko, C.M. Stafford, Thickness-dependent permeance of molecular layer-by-layer polyamide membranes, Journal of Membrane Science, 618 (2021) 118637.
[13] J. He, J.R. McCutcheon, Y. Li, Effect of different manufacturing methods on polyamide reverse-osmosis membranes for desalination: Insights from molecular dynamics simulations, Desalination, 547 (2023) 116204.
[14] P. Fu, H. Li, J. Gong, Z. Fan, A.T. Smith, K. Shen, T.O. Khalfalla, H. Huang, X. Qian, J.R. McCutcheon, L. Sun, 4D printing of polymers: Techniques, materials, and prospects, Prog. Polym. Sci., 126 (2022) 101506.
[15] M.R. Chowdhury, J. Steffes, B.D. Huey, J.R. McCutcheon, 3D printed polyamide membranes for desalination, Science, 361 (2018) 682-686.
[16] M.J. Kotelyanskii, N.J. Wagner, M.E. Paulaitis, Atomistic simulation of water and salt transport in the reverse osmosis membrane FT-30, Journal of Membrane Science, 139 (1998) 1-16.
[17] M.J. Kotelyanskii, N.J. Wagner, M.E. Paulaitis, Molecular dynamics simulation study of the mechanisms of water diffusion in a hydrated, amorphous polyamide, Comput. Theor. Polym. Sci., 9 (1999) 301-306.
[18] E. Harder, D.E. Walters, Y.D. Bodnar, R.S. Faibish, B. Roux, Molecular Dynamics Study of a Polymeric Reverse Osmosis Membrane, J. Phys. Chem. B, 113 (2009) 10177-10182.
[19] Y. Luo, E. Harder, R. Faibish, B. Roux, Computer simulations of water flux and salt permeability of the reverse osmosis FT-30 aromatic polyamide membrane, J. Membr. Sci., 384 (2011) 1-9.
[20] R. Oizerovich-Honig, V. Raim, S. Srebnik, Simulation of Thin Film Membranes Formed by Interfacial Polymerization, Langmuir, 26 (2010) 299-306.
[21] Z.E. Hughes, J.D. Gale, A computational investigation of the properties of a reverse osmosis membrane, J. Mater. Chem., 20 (2010) 7788-7799.
[22] Z.E. Hughes, J.D. Gale, Molecular dynamics simulations of the interactions of potential foulant molecules and a reverse osmosis membrane, J. Mater. Chem., 22 (2012) 175-184.

[23] V. Kolev, V. Freger, Molecular Dynamics Investigation of Ion Sorption and Permeation in Desalination Membranes, The journal of physical chemistry. B, 119 (2015).
[24] V. Kolev, V. Freger, Hydration, Porosity and Water Dynamics in the Polyamide Layer of Reverse Osmosis Membranes: a Molecular Dynamics Study, Polymer, 55 (2014).
[25] M. Ding, A. Szymczyk, F. Goujon, A. Soldera, A. Ghoufi, Structure and dynamics of water confined in a polyamide reverse-osmosis membrane: A molecular-simulation study, J. Membr. Sci., 458 (2014) 236-244.
[26] M. Shen, S. Keten, R.M. Lueptow, Dynamics of water and solute transport in polymeric reverse osmosis membranes via molecular dynamics simulations, Journal of Membrane Science, 506 (2016) 95-108.
[27] M. Shen, S. Keten, R.M. Lueptow, Rejection mechanisms for contaminants in polyamide reverse osmosis membranes, J. Membr. Sci., 509 (2016) 36-47.
[28] Y. Xiang, Y. Liu, B. Mi, Y. Leng, Hydrated Polyamide Membrane and Its Interaction with Alginate: A Molecular Dynamics Study, Langmuir, 29 (2013) 11600-11608.
[29] Y. Xiang, Y. Liu, B. Mi, Y. Leng, Molecular Dynamics Simulations of Polyamide Membrane, Calcium Alginate Gel, and Their Interactions in Aqueous Solution, Langmuir, 30 (2014) 9098-9106.
[30] W.-Y. Ahn, A.G. Kalinichev, M.M. Clark, Effects of background cations on the fouling of polyethersulfone membranes by natural organic matter: Experimental and molecular modeling study, J. Membr. Sci., 309 (2008) 128-140.
[31] T.P. Liyana-Arachchi, J.F. Sturnfield, C.M. Colina, Ultrathin Molecular-Layer-by-Layer Polyamide Membranes: Insights from Atomistic Molecular Simulations, J. Phys. Chem. B, 120 (2016) 9484-9494.
[32] T. Araki, R. Cruz-Silva, S. Tejima, K. Takeuchi, T. Hayashi, S. Inukai, T. Noguchi, A. Tanioka, T. Kawaguchi, M. Terrones, M. Endo, Molecular Dynamics Study of Carbon Nanotubes/Polyamide Reverse Osmosis Membranes: Polymerization, Structure, and Hydration, ACS Appl. Mater. Interfaces, 7 (2015) 24566-24575.
[33] W. Gao, F. She, J. Zhang, L.F. Dumée, L. He, P.D. Hodgson, L. Kong, Understanding water and ion transport behaviour and permeability through poly(amide) thin film composite membrane, J. Membr. Sci., 487 (2015) 32-39.
[34] W. Zhang, Y. Qin, W. Shi, Y. Hu, Unveiling the Molecular Mechanisms of Thickness-Dependent Water Dynamics in an Ultrathin Free-Standing Polyamide Membrane, J. Phys. Chem. B, 124 (2020) 11939-11948.
[35] L. Wang, R.S. Dumont, J.M. Dickson, Molecular dynamic simulations of pressure-driven water transport through polyamide nanofiltration membranes at different membrane densities, RSC Adv., 6 (2016) 63586-63596.
[36] Y. Song, F. Xu, M. Wei, Y. Wang, Water flow inside polamide reverse osmosis membranes: A non-equilibrium molecular dynamics study, The Journal of Physical Chemistry B, 121 (2017) 1715-1722.
[37] M.S. Jahan Sajib, Y. Wei, A. Mishra, L. Zhang, K.-I. Nomura, R.K. Kalia, P. Vashishta, A. Nakano, S. Murad, T. Wei, Atomistic simulations of biofouling and molecular transfer of a cross-linked aromatic polyamide membrane for desalination, Langmuir, 36 (2020) 7658-7668.
[38] H. Zhang, M.S. Wu, K. Zhou, A.W.-K. Law, Molecular Insights into the Composition–Structure–Property Relationships of Polyamide Thin Films for Reverse Osmosis Desalination, Environ. Sci. Technol., 53 (2019) 6374-6382.

[39] K. Li, S. Li, L. Liu, W. Huang, Y. Wang, C. Yu, Y. Zhou, Molecular dynamics simulation studies of the structure and antifouling performance of a gradient polyamide membrane, PCCP, 21 (2019) 19995-20002.
[40] J. Muscatello, E.A. Müller, A.A. Mostofi, A.P. Sutton, Multiscale molecular simulations of the formation and structure of polyamide membranes created by interfacial polymerization, J. Membr. Sci., 527 (2017) 180-190.
[41] W.D. Mulhearn, C.M. Stafford, Effects of Polyamide Chemistry on Solution Permeance in Molecular Layer-By-Layer Desalination Membranes, ACS Appl. Polym. Mater., (2022).
[42] Z. Jiang, S. Karan, A.G. Livingston, Water Transport through Ultrathin Polyamide Nanofilms Used for Reverse Osmosis, Adv. Mater., 30 (2018) 1705973.
[43] C. Jiang, L. Zhang, P. Li, H. Sun, Y. Hou, Q.J. Niu, Ultrathin Film Composite Membranes Fabricated by Novel In Situ Free Interfacial Polymerization for Desalination, ACS Appl. Mater. Interfaces, 12 (2020) 25304-25315.
[44] C.-Y. Zhu, C. Liu, J. Yang, B.-B. Guo, H.-N. Li, Z.-K. Xu, Polyamide nanofilms with linearly-tunable thickness for high performance nanofiltration, J. Membr. Sci., 627 (2021) 119142.
[45] S. Karan, Z. Jiang, A.G. Livingston, Sub–10 nm polyamide nanofilms with ultrafast solvent transport for molecular separation, Science, 348 (2015) 1347-1351.
[46] J. Yang, Z. Shen, J. He, Y. Li, Efficient separation of small organic contaminants in water using functionalized nanoporous graphene membranes: Insights from molecular dynamics simulations, J. Membr. Sci., 630 (2021) 119331.
[47] C. Fang, H. Wu, S.-Y. Lee, R.L. Mahajan, R. Qiao, The ionized graphene oxide membranes for water-ethanol separation, Carbon, 136 (2018) 262-269.
[48] D.M. Davenport, A. Deshmukh, J.R. Werber, M. Elimelech, High-Pressure Reverse Osmosis for Energy-Efficient Hypersaline Brine Desalination: Current Status, Design Considerations, and Research Needs, Environmental Science & Technology Letters, 5 (2018) 467-475.
[49] H.-G. Park, Y.-N. Kwon, Long-Term Stability of Low-Pressure Reverse Osmosis (RO) Membrane Operation—A Pilot Scale Study, Water, 10 (2018).
[50] S. Wimalawansa, Purification of Contaminated Water with Reverse Osmosis: Effective Solution of Providing Clean Water for Human Needs in Developing Countries, Int. J. Emerging Technology Adv. Engin, 9001 (2013).
[51] J. Wu, B. Jung, A. Anvari, S. Im, M. Anderson, X. Zheng, D. Jassby, R.B. Kaner, D. Dlamini, A. Edalat, E.M.V. Hoek, Reverse osmosis membrane compaction and embossing at ultra-high pressure operation, Desalination, 537 (2022) 115875.
[52] M. Shen, S. Keten, R. Lueptow, Dynamics of water and solute transport in polymeric reverse osmosis membranes via molecular dynamics simulations, Journal of Membrane Science, 506 (2016).
[53] R. Chowdhury Maqsud, J. Steffes, D. Huey Bryan, R. McCutcheon Jeffrey, 3D printed polyamide membranes for desalination, Science, 361 (2018) 682-686.
[54] W. Humphrey, A. Dalke, K. Schulten, VMD: Visual molecular dynamics, Journal of Molecular Graphics, 14 (1996) 33-38.
[55] L.J. Abbott, K.E. Hart, C.M. Colina, Polymatic: a generalized simulated polymerization algorithm for amorphous polymers, Theoretical Chemistry Accounts, 132 (2013) 1-19.
[56] J. Yang, L. Tao, J. He, J.R. McCutcheon, Y. Li, Machine learning enables interpretable discovery of innovative polymers for gas separation membranes, Sci. Adv., 8 eabn9545.

[57] S. Qiu, L. Wu, L. Zhang, H. Chen, C. Gao, Preparation of reverse osmosis composite membrane with high flux by interfacial polymerization of MPD and TMC, J. Appl. Polym. Sci., 112 (2009) 2066-2072.
[58] L. Shen, R. Cheng, M. Yi, W.-S. Hung, S. Japip, L. Tian, X. Zhang, S. Jiang, S. Li, Y. Wang, Polyamide-based membranes with structural homogeneity for ultrafast molecular sieving, Nat. Commun., 13 (2022) 500.
[59] M. Kotelyanskii, N. Wagner, M. Paulaitis, Molecular dynamics simulation study of the mechanisms of water diffusion in a hydrated, amorphous polyamide, Comput. Theor. Polym. Sci., 9 (1999) 301-306.
[60] M. Ding, Molecular simulations of reverse osmosis membranes, in, Rennes 1, 2015.
[61] E. Jones, M. Qadir, M.T. van Vliet, V. Smakhtin, S.-m. Kang, The state of desalination and brine production: A global outlook, Science of the Total Environment, 657 (2019) 1343-1356.
[62] H. Sun, S.J. Mumby, J.R. Maple, A.T. Hagler, An ab Initio CFF93 All-Atom Force Field for Polycarbonates, Journal of the American Chemical Society, 116 (1994) 2978-2987.
[63] H. Sun, Ab initio calculations and force field development for computer simulation of polysilanes, Macromolecules, 28 (1995) 701-712.
[64] H. Heinz, T.-J. Lin, R. Kishore Mishra, F.S. Emami, Thermodynamically Consistent Force Fields for the Assembly of Inorganic, Organic, and Biological Nanostructures: The INTERFACE Force Field, Langmuir, 29 (2013) 1754-1765.
[65] H. Sun, COMPASS: an ab initio force-field optimized for condensed-phase applications overview with details on alkane and benzene compounds, The Journal of Physical Chemistry B, 102 (1998) 7338-7364.
[66] S. Plimpton, Fast Parallel Algorithms for Short-Range Molecular Dynamics, Journal of Computational Physics, 117 (1995) 1-19.
[67] S. Nosé, A unified formulation of the constant temperature molecular dynamics methods, The Journal of Chemical Physics, 81 (1984) 511-519.
[68] W.G. Hoover, Canonical dynamics: Equilibrium phase-space distributions, Physical Review A, 31 (1985) 1695-1697.
[69] O. Coronell, B.J. Mariñas, D.G. Cahill, Depth Heterogeneity of Fully Aromatic Polyamide Active Layers in Reverse Osmosis and Nanofiltration Membranes, Environmental Science & Technology, 45 (2011) 4513-4520.
[70] S. Karan, Z. Jiang, G. Livingston Andrew, Sub–10 nm polyamide nanofilms with ultrafast solvent transport for molecular separation, Science, 348 (2015) 1347-1351.
[71] V. Kolev, V. Freger, Hydration, porosity and water dynamics in the polyamide layer of reverse osmosis membranes: A molecular dynamics study, Polymer, 55 (2014) 1420-1426.
[72] H. Chan, M.J. Cherukara, B. Narayanan, T.D. Loeffler, C. Benmore, S.K. Gray, S.K. Sankaranarayanan, Machine learning coarse grained models for water, Nature communications, 10 (2019) 1-14.
[73] B. Mi, O. Coronell, B.J. Mariñas, F. Watanabe, D.G. Cahill, I. Petrov, Physico-chemical characterization of NF/RO membrane active layers by Rutherford backscattering spectrometry, Journal of Membrane Science, 282 (2006) 71-81.
[74] J. Lee, C.M. Doherty, A.J. Hill, S.E. Kentish, Water vapor sorption and free volume in the aromatic polyamide layer of reverse osmosis membranes, Journal of Membrane Science, 425-426 (2013) 217-226.
[75] E.P. Chan, S.C. Lee, Thickness-dependent swelling of molecular layer-by-layer polyamide nanomembranes, Journal of Polymer Science Part B: Polymer Physics, 55 (2017) 412-417.

[76] L. Sarkisov, R. Bueno-Perez, M. Sutharson, D. Fairen-Jimenez, Materials Informatics with PoreBlazer v4.0 and the CSD MOF Database, Chem. Mater., 32 (2020) 9849-9867.
[77] S. Liu, S. Ganti-Agrawal, S. Keten, R.M. Lueptow, Molecular insights into charged nanofiltration membranes: Structure, water transport, and water diffusion, J. Membr. Sci., 644 (2022) 120057.
[78] S.H. Kim, S.-Y. Kwak, T. Suzuki, Positron Annihilation Spectroscopic Evidence to Demonstrate the Flux-Enhancement Mechanism in Morphology-Controlled Thin-Film-Composite (TFC) Membrane, Environ. Sci. Technol., 39 (2005) 1764-1770.
[79] T. Wei, L. Zhang, H. Zhao, H. Ma, M.S.J. Sajib, H. Jiang, S. Murad, Aromatic Polyamide Reverse-Osmosis Membrane: An Atomistic Molecular Dynamics Simulation, J. Phys. Chem. B, 120 (2016) 10311-10318.
[80] S. Uehara, I. Hanasaki, Y. Arai, T. Nagai, S. Kawano, Statistical characterisation of single-stranded DNA motion near glass surface beyond diffusion coefficient, Micro & Nano Letters, 9 (2014) 257-260.
[81] T.Z. Hong, L. You, M. Dahanayaka, A.W. Law, K. Zhou, Influence of Substitutional Defects in ZIF-8 Membranes on Reverse Osmosis Desalination: A Molecular Dynamics Study, Molecules, 26 (2021).
[82] F. Foglia, B. Frick, M. Nania, A.G. Livingston, J.T. Cabral, Multimodal confined water dynamics in reverse osmosis polyamide membranes, Nature Communications, 13 (2022) 2809.
[83] R.I. Urama, B.J. Mariñas, Mechanistic interpretation of solute permeation through a fully aromatic polyamide reverse osmosis membrane, J. Membr. Sci., 123 (1997) 267-280.
[84] Y. Yoon, R.M. Lueptow, Removal of organic contaminants by RO and NF membranes, J. Membr. Sci., 261 (2005) 76-86.
[85] J. He, J. McCutcheon, Y. Li, Effect of Different Manufacturing Methods on Polyamide Reverse-Osmosis Membranes for Desalination: Insights from Molecular Dynamics Simulations, SSRN Electronic Journal, (2022).
[86] L. Wang, T. Cao, J.E. Dykstra, S. Porada, P. Biesheuvel, M. Elimelech, Salt and water transport in reverse osmosis membranes: beyond the solution-diffusion model, Environmental Science & Technology, 55 (2021) 16665-16675.
[87] L. Wang, T. Cao, J.E. Dykstra, S. Porada, P.M. Biesheuvel, M. Elimelech, Salt and Water Transport in Reverse Osmosis Membranes: Beyond the Solution-Diffusion Model, Environ. Sci. Technol., 55 (2021) 16665-16675.
[88] R.E. Larson, J.E. Cadotte, R.J. Petersen, The FT-30 seawater reverse osmosis membrane--element test results, Desalination, 38 (1981) 473-483.
[89] L.B. Pártay, P. Jedlovszky, Á. Vincze, G. Horvai, Properties of Free Surface of Water−Methanol Mixtures. Analysis of the Truly Interfacial Molecular Layer in Computer Simulation, J. Phys. Chem. B, 112 (2008) 5428-5438.
[90] L.R. Pratt, A. Pohorille, Hydrophobic Effects and Modeling of Biophysical Aqueous Solution Interfaces, Chem. Rev., 102 (2002) 2671-2692.